

2013

Experimental investigation of regular fluids and nanofluids during flow boiling in a single microchannel at different heat fluxes and mass fluxes

Zachary Edel
Michigan Technological University

Follow this and additional works at: <https://digitalcommons.mtu.edu/etds>

 Part of the [Mechanical Engineering Commons](#)


Copyright 2013 Zachary Edel

Recommended Citation

Edel, Zachary, "Experimental investigation of regular fluids and nanofluids during flow boiling in a single microchannel at different heat fluxes and mass fluxes", Dissertation, Michigan Technological University, 2013.

<https://doi.org/10.37099/mtu.dc.etds/691>

Follow this and additional works at: <https://digitalcommons.mtu.edu/etds>

 Part of the [Mechanical Engineering Commons](#)

EXPERIMENTAL INVESTIGATION OF REGULAR FLUIDS AND
NANOFLUIDS DURING FLOW BOILING IN A SINGLE MICROCHANNEL
AT DIFFERENT HEAT FLUXES AND MASS FLUXES

By

Zachary J. Edel

A DISSERTATION

Submitted in partial fulfillment of the requirements for the degree of

DOCTOR OF PHILOSOPHY

In Mechanical Engineering-Engineering Mechanics

MICHIGAN TECHNOLOGICAL UNIVERSITY

2013

This dissertation has been approved in partial fulfillment of the requirements for the Degree of DOCTOR OF PHILOSOPHY in Mechanical Engineering-Engineering Mechanics

Department of Mechanical Engineering-Engineering Mechanics

Dissertation Advisor: *Abhijit Mukherjee*

Committee Member: *Jeffrey Allen*

Committee Member: *Desheng Meng*

Committee Member: *Jason Keith*

Department Chair: *William Predebon*

Table of Contents

| | |
|---|-----------|
| Abstract..... | 4 |
| 1 Introduction..... | 5 |
| 1.1 Motivation..... | 6 |
| 1.2 Objectives | 10 |
| 2 Literature Review..... | 10 |
| 2.1 Flow Regime Transition | 11 |
| 2.2 Forces Acting at the Liquid-Vapor Interface..... | 12 |
| 2.3 Bubble Dynamics..... | 22 |
| 2.4 Stability Considerations..... | 26 |
| 2.5 Influence of Nanofluids | 34 |
| 3 Methods..... | 42 |
| 4 Results and Discussion..... | 46 |
| 4.1 Location of the Onset of Bubble Elongation (OBE)..... | 46 |
| 4.2 Bubble Growth Rates..... | 53 |
| 4.3 Flow Regime Transition Cycle Images | 61 |
| 4.4 Phase Records | 70 |
| 4.5 Cycle Duration and Bubble Frequencies | 77 |
| 4.6 Future Work..... | 80 |
| 5 Conclusions..... | 83 |
| 6 References..... | 85 |

Abstract

The dissipation of high heat flux from integrated circuit chips and the maintenance of acceptable junction temperatures in high powered electronics require advanced cooling technologies. One such technology is two-phase cooling in microchannels under confined flow boiling conditions. In macroscale flow boiling bubbles will nucleate on the channel walls, grow, and depart from the surface. In microscale flow boiling bubbles can fill the channel diameter before the liquid drag force has a chance to sweep them off the channel wall. As a confined bubble elongates in a microchannel, it traps thin liquid films between the heated wall and the vapor core that are subject to large temperature gradients. The thin films evaporate rapidly, sometimes faster than the incoming mass flux can replenish bulk fluid in the microchannel. When the local vapor pressure spike exceeds the inlet pressure, it forces the upstream interface to travel back into the inlet plenum and create flow boiling instabilities. Flow boiling instabilities reduce the temperature at which critical heat flux occurs and create channel dryout. Dryout causes high surface temperatures that can destroy the electronic circuits that use two-phase micro heat exchangers for cooling.

Flow boiling instability is characterized by periodic oscillation of flow regimes which induce oscillations in fluid temperature, wall temperatures, pressure drop, and mass flux. When nanofluids are used in flow boiling, the nanoparticles become deposited on the heated surface and change its thermal conductivity, roughness,

capillarity, wettability, and nucleation site density. It also affects heat transfer by changing bubble departure diameter, bubble departure frequency, and the evaporation of the micro and macrolayer beneath the growing bubbles.

Flow boiling was investigated in this study using degassed, deionized water, and 0.001 vol% aluminum oxide nanofluids in a single rectangular brass microchannel with a hydraulic diameter of 229 μm for one inlet fluid temperature of 63°C and two constant flow rates of 0.41 ml/min and 0.82 ml/min. The power input was adjusted for two average surface temperatures of 103°C and 119°C at each flow rate. High speed images were taken periodically for water and nanofluid flow boiling after durations of 25, 75, and 125 minutes from the start of flow. The change in regime timing revealed the effect of nanoparticle suspension and deposition on the Onset of Nucleate Boiling (ONB) and the Onset of Bubble Elongation (OBE). Cycle duration and bubble frequencies are reported for different nanofluid flow boiling durations. The addition of nanoparticles was found to stabilize bubble nucleation and growth and limit the recession rate of the upstream and downstream interfaces, mitigating the spreading of dry spots and elongating the thin film regions to increase thin film evaporation.

1 Introduction

Efficient thermal-fluid systems are needed to minimize energy waste and reduce emission of the green-house gases that are responsible for global warming. An

ever-increasing growth of industries in the developing world demands improved heat exchange systems with heat removal capacities well above the present limit of 250 W/cm^2 in order to limit the carbon footprint and satisfy domestic and international regulations. Nanoparticles suspended in different base fluids can alter the momentum and heat transfer characteristics of the velocity and thermal boundary layers by significantly increasing the liquid viscosity and thermal conductivity. Additions of nanoparticles have been found to effectively improve the Critical Heat Flux (CHF) at which nucleate boiling transitions to film boiling. An increase in CHF can result in the design of more efficient and compact heat exchangers for the nuclear and chemical industries, Heating, Ventilation and Air-Conditioning (HVAC) systems, electronic systems, high heat flux lasers, X-rays and optical devices.

1.1 Motivation

Computers and specialized electronic devices have become a vital part of life in many countries around the world. As these devices continue to advance, both in capability and compactness, thermal management is becoming a limiting factor in electronics design. The advancement of computing technology has been growing exponentially for more than three decades, following a trend identified by Gordon Moore in 1965. Moore's law describes a doubling in the number of transistors that can be placed on an integrated circuit every two years. The average power density

of single-core microprocessors is expected to increase from 100 W/cm^2 in 2005 to 1000 W/cm^2 by 2015 [Krishnan, et al., 2007].

As the need for advanced processing and data storage technology advances, data centers are becoming an indispensable resource in nearly every sector of the economy, such as manufacturing, universities, financial services, and government institutions. The energy consumed by data centers represents almost 2% of the world electricity consumption and is growing by 15% annually. As the cooling process becomes the major part of data center operating costs, advancement in cooling technology is critical for the reduction of greenhouse gas emissions such as CO_2 [Thome and Cioncolini, 2010].

The dissipation of high heat flux from integrated circuit chips and the maintenance of acceptable junction temperatures require advanced cooling technologies. Micro heat exchangers have become one of the most effective cooling techniques for high-power density, compact applications [Zhao and Lu, 2002]. They are used in high-speed processor chips, microprocessors, high-powered lasers, cutting-edge power and switching devices, and lightweight cooling applications like satellites, avionics, and portable computers [Qu and Mudawar, 2004].

Two-phase flow in micro heat exchangers can achieve significantly higher heat flux than single phase flow due to the latent heat of vaporization. Heat transfer coefficients for flow boiling in microchannels can exceed $100,000 \text{ W/m}^2 \text{ }^\circ\text{C}$, compared to $10,000 \text{ W/m}^2 \text{ }^\circ\text{C}$ for single-phase flow [Kandlikar, et al., 2006]. Different mechanisms govern flow boiling heat transfer on a microscale because

surface tension and intermolecular forces dominate gravity forces [Kandlikar, 2004].

Heat is dissipated from a surface during boiling by two modes: latent and sensible heat transfer. Latent heat transfer corresponds to the energy required to transform a liquid into a gas. Sensible heat transfer corresponds to the energy that is removed by a liquid during direct conduction or convection. In pool boiling, the vapor bubbles that form near the heated surface merge together and contract, drawing cooler liquid toward the wall and enhancing sensible heat transfer [Mukherjee and Dhir, 2004].

In macroscale flow boiling, bubbles will nucleate on the channel walls, grow, and depart from the surface when they reach a critical departure radius that is determined by buoyancy and bulk flow drag forces. In microscale flow boiling, gravity is generally negligible and bubbles can fill the channel diameter before the liquid drag force has a chance to sweep them off of the channel wall. As a confined bubble elongates in the channel, it traps thin liquid films between the heated wall and the vapor core that are subject to large temperature gradients [Mukherjee and Kandlikar, 2005]. The thin films evaporate rapidly, sometimes faster than the incoming mass flux can replenish bulk fluid in the microchannel. The enhancement of latent heat transfer causes an explosion of vapor pressure. When the local vapor pressure spike exceeds the inlet pressure, it can force the upstream interface to travel back into the inlet plenum and create flow boiling instabilities [Kandlikar, et al., 2001].

Flow boiling instabilities can reduce the temperature at which critical heat flux occurs and create channel dryout. Dryout causes high surface temperatures that can destroy the electronics that two-phase micro heat exchangers are used to cool. The mechanisms behind flow boiling instability, bubble nucleation, and bubble growth must be understood in order to better design micro heat exchangers.

Several innovations have been shown to reduce flow instabilities; these include introducing pressure drop elements at the channel inlet, manufacturing artificial nucleation sites at desired locations inside the microchannels, using diverging channels to aid in bubble evacuation, using a porous membrane to allow vapor to exit the microchannel side wall, and using a triangular or trapezoidal channel cross section to allow for stable annular flow. However, each of these solutions has inherent drawbacks such as increased power consumption, difficulty to manufacture, and decreased surface area to volume ratio.

Suspending nanoparticles of sizes below 50 nm in fluids can enhance convective heat transfer; these nanoparticle suspensions are called nanofluids [Choi, 1995]. The nanofluids are considered as next generation heat transfer fluids because they present improved heat transfer properties as compared to pure liquids. The large surface area-to-volume ratio of the nanoparticles helps to enhance the stability of the suspensions. If effectively employed, the nanofluids can aid in the development of compact heat exchangers capable of removing ultra-high heat flux.

The main advantages of two-phase cooling are very high heat transfer coefficients at low vapor quality, increase of heat transfer coefficient with heat flux,

and nearly constant footprint temperature due to the combined effects of a decrease in saturation temperature and heat transfer coefficient along the channel length.

Thin film evaporation around the microbubbles generated during flow boiling is further enhanced by nanoparticles that significantly increase thermal conductivity of the thin film as well as the wettability of the microchannel surfaces.

1.2 Objectives

The objective of the current study is to increase nucleation site density and the lateral wicking of fluids into the thin film regions of the evaporating meniscus by adding nanoparticles to the two-phase boiling process in a single microchannel. Increased wicking of fluids into the thin film regions will counteract the evaporation recoil force at the triple point and cause a slower recession of the liquid interface due to the dry patch under a vapor bubble growing more slowly.

The current study aims to prove that the effect of surface modifications due to nanoparticle deposition will cause an advantageous change in the flow regime transition cycle for the stabilization of microchannel flow boiling. Two independent values of surface temperature and flow rate are tested to prove that flow regime transition is more stable at lower surface temperatures and higher flow rates.

2 Literature Review

An in-depth understanding of bubble and contact line dynamics and surface and fluid property modifications is necessary for the design of compact heat exchangers

that utilize the flow boiling of nanofluids. Wall heat transfer inside microchannels during flow boiling is primarily achieved by thin film evaporation and nucleate boiling mechanisms at the receding and advancing contact regions, respectively, of the elongated vapor bubbles. Detailed numerical calculations [Mukherjee, 2007] show that flow boiling in microchannels is inherently a conjugate heat transfer problem and the bulk of the heat flow takes place through the channel sidewalls into the liquid film surrounding the bubbles. The current project is aimed to improve nanofluid-based two-phase heat exchanger efficiency in order to reduce energy consumption and significantly lessen the emission of green house gases and the carbon footprint of a host of electronics and related industries.

2.1 Flow Regime Transition

Huo et al. reported six different flow patterns for flow boiling in small diameter tubes of 2.01 mm to 4.26 mm in diameter: dispersed bubble flow, bubbly flow, slug flow, churn flow, annular flow, and mist flow [Huo et al., 2004]. Dispersed bubble flow is generally not distinguished from bubbly flow in microchannels due to the small channel diameter. When departed bubbles are carried downstream, they coalesce and form vapor plugs. Under conditions of high wall superheat, the bubbly flow regime quickly becomes slug flow and eventually annular flow [Lu and Pan, 2008]. If wall superheat is high enough, the channel will dry out and surface temperatures will soar.

Flow regimes generally alternate in a cyclic pattern during flow boiling in microchannels. Wu and Cheng observed three unstable boiling modes for water in a parallel channel micro heat exchanger having channels of trapezoidal cross-section and a hydraulic diameter of $186\mu\text{m}$: (1) liquid/two-phase alternating flow (LTAF), (2) continuous two-phase flow (CTF), and (3) liquid/two-phase/vapor alternating flow (LTVAF) [2004].

After the onset of nucleate boiling, the pressure drop across the microchannels suddenly increased due to the generation of vapor bubbles. The increase in pressure drop caused a decrease in mass flux, which in turn decreased the pressure drop. This scenario explains the oscillation of pressure and mass flux. During the interval when mass flux was increased, the constant wall heat flux was insufficient to boil the coolant and single-phase liquid appeared. When the mass flux decreased again, the constant heat flux boiled the coolant and two-phase flow or vapor phase appeared again. Large amplitude, long period oscillations of coolant and wall temperatures resulted from the alternating appearance of flow patterns during LTAF and LTVAF boiling modes.

2.2 Forces Acting at the Liquid-Vapor Interface

Flow reversal in a microchannel occurs due to rapid bubble growth when the combined effects of vapor pressure and evaporation momentum-change at the upstream liquid-vapor interface overcome the combined effects of the incoming

liquid pressure, the incoming liquid inertia, and the capillary forces that act at the contact line (see Figure 2.2.1).

Equation 1 shows the balance of forces per unit length acting at the liquid-vapor interface.

$$\sum F_{\text{interface}} = (F_{P,\text{liq}} + F_{I,\text{liq}} + F_S) - (F_{P,\text{vap}} + F_M) \quad \text{Equation 1}$$

$F_{P,\text{liq}}$ is due to the pressure of incoming liquid, $F_{I,\text{liq}}$ is due to the inertia of the incoming liquid, F_S is due to the surface tension (capillary forces) at the interface, $F_{P,\text{vap}}$ is due to the vapor pressure, and F_M is due to the evaporation momentum change. The incoming liquid pressure and capillary forces remain fairly constant, but the local vapor pressure and evaporation momentum-change at the upstream interface both increase as a vapor bubble grows.

As the fluid evaporates at the liquid-vapor interface, the difference in densities between the two phases causes the vapor molecules to leave the interface at a much higher velocity than the liquid molecules traveling toward it. The resulting change in momentum creates an evaporation momentum force on the liquid vapor interface. The force per unit length due to the evaporation momentum change at the interface is given by

$$F'_M = \left(\frac{q}{h_{lv}} \right)^2 \frac{D}{\rho_v} \quad \text{Equation 2}$$

Where q is the wall heat flux, h_{lv} is the latent heat of evaporation, D is the hydraulic diameter, and ρ_v is the density of the vapor phase.

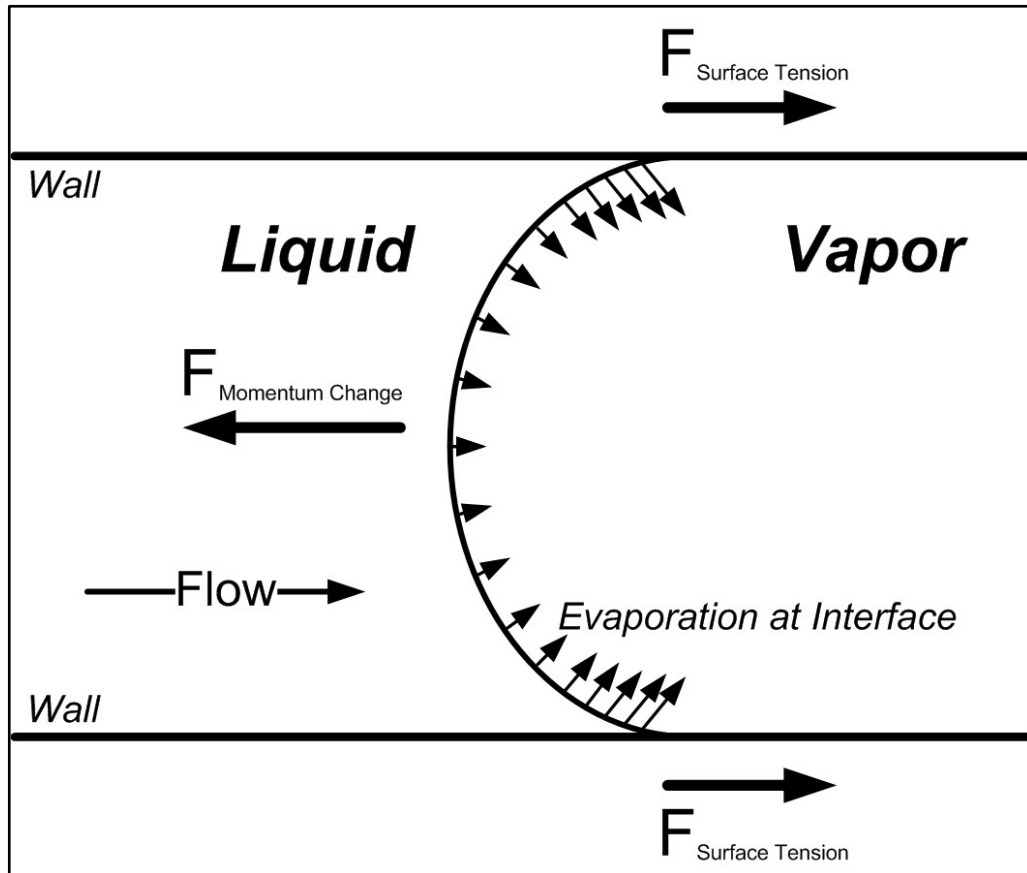


Figure 2.2.1: Forces acting at the liquid-vapor interface for confined flow boiling. Thin film evaporation plays a dominant role in interface movement when flow is confined.

Fluid molecules in the bulk liquid form chemical bonds with one another, which contain a certain amount of binding energy. Molecules at the surface of the liquid vapor interface cannot form as many bonds because there are much fewer molecules in the vapor phase. The lack of chemical bonds at the liquid-vapor interface results in a higher energy for the surface molecules. This energy is called surface tension,

and causes the interface to take on some curvature, depending on the make-up of the liquid, the vapor, and the solid surface at a microchannel wall [Bruus, 2008].

Surface tension creates a force at the triple-point contact line around the perimeter of the channel. The force per unit length due to surface tension is given by

$$F'_S = \sigma \cos \theta \quad \text{Equation 3}$$

Where σ is the surface tension and θ is the contact angle.

Since the vapor in a growing bubble has a much lower density than the liquid, it forces the liquid molecules away from it. The inertia of the liquid molecules acts to suppress the growth of a vapor bubble. When the liquid is moving through the channel at velocity V , the force per unit length at the interface due to the inertia of the fluid is given by

$$F'_I = \rho_l V^2 D = \frac{G^2 D}{\rho_l} \quad \text{Equation 4}$$

Where G is the mass flux and ρ_l is the density of the liquid phase. If the local vapor pressure in the bubble overcomes the inlet pressure and forces the upstream interface toward the channel inlet, the inertia force takes a different form, but still acts against the movement of the interface due to the necessity to accelerate the liquid.

The buoyancy force acting on a bubble due to gravity is given by

$$F'_g = (\rho_l - \rho_v)gD^2 \quad \text{Equation 5}$$

Where g is acceleration due to gravity. This force is generally negligible compared to the other forces that act on the bubble and may be neglected when dealing with confined flow in microchannels. Viscous forces also play a role in bubble motion because moving interfaces causes liquid to flow. Viscous forces always act in the opposite direction as the fluid motion. If a slug of liquid is being forced upstream or downstream by a moving interface, friction will act to impede the interface motion.

The pressure drop across a curved interface can be derived as a function of surface tension and curvature using an energy minimum condition for the free surface energy and solving for the pressure drop. The result is the Young-Laplace equation,

$$\Delta P_{surface} = \left(\frac{1}{R_1} + \frac{1}{R_2} \right) \sigma \quad \text{Equation 6}$$

R_1 and R_2 are the characteristic radii of curvature for the surface; the radius of curvature in a direction is taken as positive when the surface is concave as seen from the gas, and as negative when it is convex as seen from the gas. For a meniscus in contact with a solid surface in a microchannel, there is a surface tension associated with each of the solid/liquid, solid/gas, and liquid/gas interfaces. The liquid and gas phases adjust to balance the surface tension forces and an angle is formed between the liquid/gas interface and the solid surface. The contact angle, θ ,

is measured through the liquid at the point where the three phases meet. Accounting for the change in curvature of a meniscus in a microchannel due to the contact angle, the radius of curvature can be calculated using trigonometry as:

$$R_i = \frac{a_i}{\cos \theta_i} \quad \text{Equation 7}$$

Where a_i is the half-dimension of surface i that makes contact with the meniscus. If the microchannel is round, a_i is the radius of the tube. Inserting Equation 7 into Equation 6, the change in pressure across a liquid-vapor interface in a rectangular microchannel can be calculated by

$$\Delta P_{surface} = \left(\frac{\cos \theta_1}{a_1} + \frac{\cos \theta_2}{a_2} \right) \sigma \quad \text{Equation 8}$$

From Equation 8, it can be seen that capillary forces are affected by the surface wettability (θ_i), the channel dimensions (a_i), and the value of surface tension (σ), which can vary with temperature and surfactant concentration.

The wetting properties of a surface for a given liquid can affect the motion of a vapor bubble by modifying the solid/liquid interfacial energy, which changes the balance between solid/liquid, solid/gas, and liquid/gas surface tension forces. If a gradient in wettability exists in a microchannel, it can induce bubble motion from the more hydrophobic region to the more hydrophilic region [Squires and Quake, 2005]. This effect has been used to transport CO₂ bubbles in micro-direct methanol

fuel cells to remove it from the system and to create a self-pumping methanol delivery system [Meng and Kim, 2009].

The magnitude of surface tension depends on fluid temperature and can depend on surfactant concentration if one is present. When a temperature gradient is present in a microchannel, the capillary forces acting along the interfaces of a vapor bubble can become unbalanced and induce bubble motion. In the case of flow boiling, conjugate heat transfer between channels can create temperature gradients along the width and length of a microchannel, and conjugate heat transfer between the heated wall and the non-uniformly evaporating liquid can create temperature gradients along the axis of a microchannel [Mukherjee, 2007]. Temperature gradients also exist along the liquid-vapor interface due to the motion of sub-cooled liquid around a bubble that is growing off of a super-heated channel wall. Temperature gradients along the liquid-vapor interface create a surface tension gradient force, known as the Marangoni force,

$$F_{Maran} = \nabla \sigma \quad \text{Equation 9}$$

This force is responsible for the Marangoni effect, which is characterized by the circulation of liquid around the base of a bubble or interface. The Marangoni effect can also be induced by inhomogeneities of surfactant concentration, which create a surface tension gradient along the liquid-vapor interface [Kostarev, et al., 2006].

Chamarthy et al. [2008] studied the convection patterns present in an evaporating meniscus of methanol in three circular glass tubes at room temperature

with diameters of 75, 200, and 400 μm . A toroidal vortex was observed near the meniscus interface; it was symmetric in the 75 μm tube, slightly asymmetric in the 200 μm tube, and very asymmetric in the 400 μm tube. These results indicate that Marangoni convection may play a significant role in vapor bubble growth during flow boiling in microchannels due to the effects of transient conduction around the base of a growing vapor bubble and the resulting change in local fluid temperature near the liquid-vapor interface away from the heated wall.

As can be seen in Equation 6, curvature is the key parameter in determining the magnitude of pressure drop across a liquid-vapor interface. Since pressure drop is inversely proportional to the radius of curvature, a confined bubble with unequal radii of curvature at the left and right interfaces will move in the direction of increasing radius. Assuming a constant contact angle, the curvature of an interface is determined by the channel diameter. Bubble motion can be induced in a microchannel by introducing a gradient in channel diameter. Parallel channel test sections with diverging cross-section channels have been shown to stabilize flow boiling in microchannels by forcing the vapor bubbles in the direction of divergence [Lee and Pan, 2008; Lu and Pan, 2008].

Kandlikar [2004] proposed two new non-dimensional groups to relate the magnitude of the evaporation momentum force acting at the liquid vapor interface to inertial and surface tension forces.

$$K_1 = \left(\frac{q}{G \cdot h_{lv}} \right)^2 \frac{\rho_l}{\rho_v} \quad \text{Equation 10}$$

$$K_2 = \left(\frac{q}{h_{lv}} \right)^2 \frac{D}{\rho_v \sigma} \quad \text{Equation 11}$$

K_1 represents the ratio of evaporation momentum force to the inertia force; a high value of K_1 indicates that the evaporation momentum forces are dominant and are likely to alter interface movement. K_2 represents the ratio of the evaporation momentum force to the surface tension force. The non-dimensional group K_2 governs the movement of the interface at the contact line. A high value of K_2 indicates that the evaporation momentum force will cause the interface to overcome the retaining surface tension force and bubble movement will occur. The contact angle is not included in the ratio for K_2 , although it may involve more complex dependence on dynamic contact angle and surface orientation.

Derjaguin [1992] provided the basic mechanism of the thin film behavior by showing that the net effect, at the macroscopic level, of solid-liquid interactions is a reduction of pressure of the liquid interface relative to the pressure of the equilibrium vapor phase. He argued that the disjoining action could explain the deviation from the laws of hydrostatics that exists in a thin wetting film. There is an extensive amount of literature available on thin film evaporation. Peter C. Wayner, Jr. developed a widely accepted model for the behavior of the liquid meniscus. He modeled the meniscus using some well-established techniques and created a set of

governing equations that can be used to predict the fluid dynamics and heat transfer of a liquid meniscus. He also hypothesized that the steady evaporating meniscus can be used to sustain very high heat fluxes [Dasgupta, et al., 1994; Dasgupta, et al., 1993; Potash and Wayner, 1972; Sujanani and Wayner, 1992; Wayner and LaCroix, 1976].

Mukherjee and Kandlikar [2006] numerically simulated a moving evaporating meniscus and obtained details of the heat transfer and fluid flow near the contact region. The heat transfer from the wall was found to be the highest near the advancing contact region due to transient heat conduction. Jacobi and Thome [2002] presented a model for heat transfer during elongated bubble flow regime inside a microchannel. The model assumed thin-film evaporation to be the dominant heat transfer mechanism. The model required judicious choice of two important parameters: the effective nucleation superheat and the initial thin film thickness. Mukherjee [2009] recently compared heat transfer mechanisms present during flow boiling inside microchannels with nucleate pool boiling and a moving evaporating meniscus. It was concluded that thin film evaporation is the primary heat transfer mechanism during flow boiling inside microchannels though it gave rise to an apparent notion of presence of nucleate boiling mechanism.

During microlayer evaporation, flow and heat transfer are coupled with the capillary force, intermolecular interactions (disjoining pressure), and fluid surface interactions (wetting phenomena). The structural disjoining pressure is a long-range force that acts normal to the wall and arises due to the ordering of particles in the

confinement of the thin film region, as opposed to their greater freedom of motion in the bulk liquid. The arrangement of the particles gives rise to an excess pressure in the film, which has an oscillatory decay profile with the film thickness. The structuring force introduced by the addition of nanoparticles to the thin film region of an evaporating meniscus exhibits an improved spreading capability of nanofluids in confined spaces and has been observed to change the macroscopic contact angle of a liquid droplet, stabilize liquid films, and lift an oil droplet from a wall in an aqueous solution. The enhanced spreading capability can increase the rewetting ability of a fluid in boiling. The concept of structural disjoining pressure could be used to explain microlayer dynamics such as the pinning of the contact line of a meniscus. The difference between thermal nanofluids and pure liquids lies in the zone where the conventional disjoining pressure becomes negligible and the structural disjoining pressure becomes important [Wen, 2008].

2.3 Bubble Dynamics

Flow boiling instability can be attributed at the most basic level to rapid bubble growth. In order to attenuate instability during flow boiling in microchannels, bubble nucleation and growth must be well understood. Kandlikar [2004] determined that the role of the convective boiling mechanism is diminished in microchannels and that heat transfer is dominated by nucleate boiling. Yen et al. [2006] found that nucleate boiling was the dominant form of heat transfer for vapor qualities less than 0.4 in both square and circular microchannels, and that the local

heat transfer coefficient was significantly higher for nucleate boiling than for convective boiling. Due to the high heat transfer coefficient in microchannels, the bulk liquid is heated much faster than in macrochannels and may become superheated before the phase change process takes place [Kandlikar, 2006]. A superheated environment leads to rapid bubble growth, which contributes to flow boiling instability. Controlling bubble nucleation and growth rate by initiating the phase change process before the bulk liquid is overheated can greatly enhance micro heat exchanger performance.

The minimum wall superheat required to induce nucleation rapidly increases as the channel diameter and the nucleation cavity radius decreases [Kandlikar, 2004; Peng, et al., 1998]. In order to design effective micro heat exchangers, surface properties should be chosen so that a maximum number of microcavities will have an optimal radius to nucleate vapor bubbles. The critical nucleation cavity radii are determined by assuming that bubble growth will occur when the coldest liquid temperature encountered on the interface exceeds the saturation temperature corresponding to the vapor pressure inside the bubble [Kandlikar, 2006]. Assuming a linear temperature gradient in the liquid from the channel wall, this occurs at the top of the bubble.

Kandlikar et al. [1997] performed a numerical simulation of a bubble growing in a minichannel and determined that the location of the streamline at $y=y_s$ is at $y=1.1r_b$. Based on this finding, the minimum and maximum cavity radii that will

nucleate vapor bubbles for a given wall superheat is given by

$$\{r_{c,\min}, r_{c,\max}\} = \frac{\delta_l \sin \theta_r}{2.2} \left(\frac{\Delta T_{sat}}{\Delta T_{sat} + \Delta T_{sub}} \right) \times \left[1 \pm \sqrt{1 - \frac{8.8 \sigma T_{sat} (\Delta T_{sat} + \Delta T_{sub})}{\rho_v h_{lv} \delta_l \Delta T_{sat}^2}} \right] \quad \text{Equation 12}$$

Where the thickness of the liquid sublayer is given by $\delta_l = k_L/h$. The critical radius that will nucleate bubbles first for a given surface temperature and subcooling is found by setting the radical in Equation 13 equal to zero. The wall superheat required to nucleate bubbles for a given cavity radius is given by

$$\Delta T_{sat}|_{ONB} = \frac{1.1 r_c q}{k_l \sin \theta_r} + \frac{2 \sigma \sin \theta_r}{r_c} \frac{T_{sat}}{\rho_v h_{lv}} \quad \text{Equation 13}$$

Using the above criteria, one can estimate the effects of surface roughness and artificially fabricated nucleation cavities on micro heat exchanger performance. Peng et al. [1998] presented minimum heat flux and wall superheat criteria for bubble nucleation as a function of channel hydraulic diameter. Li and Cheng [2004] showed that nucleation temperature decreased as the contact angle increased. High mass flow rates were shown to suppress bubble nucleation, whereas high heat fluxes were shown to promote bubble nucleation. Yen et al. [2006] observed that the corners of a square cross-section channel were observed to act as effective active nucleation sites.

Li et al. [2004] identified two bubble growth trends for bubble radii less than the channel diameter: linear growth, suggesting the bubble growth is inertia controlled, and growth that follows the square root of time, indicating that the growth may be diffusion controlled. Lee et al. [2004] reported bubble growth rate to be isotropic

for bubble radii smaller than the channel diameter. As the bubble radius grew larger than the channel diameter, it was limited by both top and bottom walls and was significantly affected by the flow drag.

Chang and Pan [2007] observed bubble growth in parallel microchannels after the bubble reached the channel diameter. A bubble would nucleate, evolve into a bubble slug, detach from the wall, and grow exponentially in the streamwise direction as it was swept downstream by the incoming liquid. While attached to the wall, surface tension tended to keep the bubble in place and elongate the bubble by counteracting with the drag of the bulk flow. When the bubble detached from the wall, it decreased in length due to a change in shape before continuing to grow. Bubble length was observed to grow exponentially. Lee and Pan [2008] observed bubble growth rate in a diverging cross-section channel to be higher than for a uniform cross-section channel.

Edel and Mukherjee [2009] observed that bubble growth rates in a single microchannel for radii larger than the channel diameter varied about a mean that increased with increasing wall superheat. The increase in local fluid pressure from an expanding bubble suppressed the growth of a neighboring bubble. Wang and Cheng, [2009] observed the acceleration of liquid flow around two growing vapor bubbles due to the decrease in effective cross-sectional area. Hetsroni et al. [2003] and [2004] reported temporal variation of bubble size in both streamwise and spanwise directions. Revellin et al. [2008] observed that bubbles travel faster as they grow in size, until they reach a certain length when the velocity plateaus and

remains constant. A difference in elongated bubble velocity and length explains the merging of vapor bubbles in a microchannel. Mukherjee and Dhir [2004] showed that the merger of multiple vapor bubbles in nucleate pool boiling increased the wall heat transfer by trapping a liquid layer between the bubble bases during merger and by drawing cooler liquid towards the wall during contraction after merger.

2.4 Stability Considerations

Flow boiling instability is characterized by periodic oscillation of flow regimes which induce oscillations in fluid temperature, wall temperatures, pressure drop, and mass flux. Chang and Pan [2007] used flow reversal into the inlet plenum as the criterion to identify the existence of instability. There are two main phenomena that contribute to flow boiling instability: parallel channel instability and upstream flow loop compressibility. It is advantageous to consider the channel pressure drop demand curve in analyzing the effects of each type of instability. At high mass flux, liquid single-phase flow exists and the pressure drop increases with mass flux. As the mass flux decreases and the heat flux is held constant, the Onset of Nucleate Boiling (ONB) occurs and two-phase flow is initiated. As mass flux decreases further, the pressure decreases until the Onset of Flow Instability (OFI) occurs and the pressure drop begins to increase with decreasing mass flux. In this region, the flow is not necessarily unstable, but may be susceptible to instability if the pump is not able to supply sufficient pressure to compensate perturbations in mass flux.

When mass flux is decreased further, eventually the flow will transition to single-phase vapor and the pressure drop will decrease with decreasing mass flux again.

A channel is susceptible to flow excursion (or Ledinegg) instability when the slope of the demand pressure drop-mass flux curve is smaller in magnitude than the loop supply pressure drop-mass flux curve [Zhang, et al., 2009],

$$\left. \frac{\partial(\Delta P)}{\partial G} \right|_{\text{channel_demand}} \leq \left. \frac{\partial(\Delta P)}{\partial G} \right|_{\text{pump_supply}} \quad \text{Equation 14}$$

When a constant displacement pump such as a syringe pump is used, the slope of the pump supply curve is almost infinite because the mass flow rate is fixed regardless of pressure drop. In most cases, however, there is a small amount of tubing between the pump and the channel and the channel is often connected to other parallel channels using common inlet and outlet headers. These factors influence the slope of the pump supply curve experienced at the inlet of a given channel because they introduce upstream flow compressibility and channel-to-channel interactions.

In a single-channel test section with no upstream compressibility, the pump supply curve can be applied directly to the channel inlet. As a bubble grows in the channel, mass flux backs up in the inlet header and forces the bubble out of the channel. When multiple channels are introduced, the mass flux in adjacent channels can increase to compensate for the decreased mass flux in a channel with an expanding bubble. This effectively decreases the magnitude of the pump supply

curve slope for a given channel because the pressure increase that would be experienced by a given channel is dissipated in adjacent channels which compensate the pressure rise by an increase in local mass flux. Considering a constant displacement pump, a single channel would have an infinite-slope pump supply curve, whereas a test section with an infinite number of parallel channels would have a zero-slope pump supply curve. In the case of infinite channels, any local pressure spike that exceeds the constant pressure drop between headers would cause flow instability. Channel-to-channel instability thus increases with increasing number of channels.

Flow loop compressibility can be introduced to a system through compliant tubing, movement of rigid components, trapped gas bubbles, and large liquid volumes where minute changes in fluid density may become significant. If compressibility exists upstream of an expanding bubble in a microchannel, the mass flux and pressure drop experienced by the microchannel can vary when the local pressure spikes due to vapor production. Instability due to upstream flow loop compressibility can be understood by considering the accumulation of fluid in the flow loop upstream of the microchannel and the effect of changing mass flux on heat transfer to the fluid.

Lee and Yao [2009] studied system instability due to flow loop compressibility in evaporative microchannels using a flow loop that consisted of a constant displacement pump, a buffer tank that allowed the accumulation of fluid, a constant

heat flux pre-heater, and a parallel-channel test section. The system instability process was described sequentially as follows:

1. When the experiment was started, liquid flowed through the test section and the heaters were turned off so that all of the channels were occupied by single phase liquid flow.

2. The test section heaters were turned on and the bulk temperature of the liquid was increased beyond the saturation temperature near the exit. The wall temperatures exceeded the limit for incipient boiling and the boiling process began in the microchannels.

3. As the boiling occurred, the pressure drop across the channels increased and raised the pressure of the inlet header. As a result, the buffer tank gradually filled with liquid while the flow through the test section was reduced. Since the pre-heater provided a constant heat flux, the bulk temperature of the fluid at the inlet increased and the boiling became more severe. This positive-feedback scenario was self-propelling.

4. When the tank was fully pressurized, fluid could no longer enter it and the flow rate through the test section increased back to that of the supply pump. If stable conditions were achieved at this point, the flow would become equilibrated and steady state conditions would be reached.

5. If unstable conditions existed, the bubbles would back up into the inlet header and warm the surrounding fluid. When the liquid film of the elongated bubbles dried up, the channels were occupied by single-phase vapor and little vapor

expansion occurred. The pressure drop decreased again so that the mass flux in the channel increased and the bubbles were washed away by incoming liquid.

6. The increase in mass flux caused the bulk fluid temperature at the inlet to decrease due to the constant heat flux pre-heater. The decrease in bulk fluid temperature and the increase in mass flux caused the vapor generation in the channel to decrease and the flow became primarily single-phase liquid.

7. After the excess liquid in the buffer tank was mostly discharged, the tank pressure diminished and the flow rate through the microchannel decreased. This increased the bulk fluid temperature at the inlet and allowed the fluid to heat up in the channel and re-initiate incipient boiling.

8. The boiling caused the fluid to accumulate in the tank again and the cycle repeated.

Upstream flow loop compressibility instability is also called flow regime transition instability because the transition of flow regimes is responsible for the oscillation in flow parameters. Oscillations in surface temperatures, fluid temperatures, pressure drop, and mass flux have been directly correlated with flow regimes and help explain the transient phenomena [Wang and Cheng, 2008; Lee and Yao, 2009; Huh, et al., 2007; Wang, et al., 2007; Wu and Cheng, 2004; Xu, et al., 2005]. Long-period oscillations have been associated with upstream compressibility instability, whereas short-period oscillations have been associated with channel-to-channel and rapid bubble growth instabilities. Alternating flow boiling regimes create oscillations in coolant temperature, wall temperature, pressure drop, and mass

flux. A Fast Fourier Transform, performed by Lee et al. [2006] has shown the temperature and pressure fluctuations that occur in Microchannel flow boiling to be periodic in nature with a single dominant frequency.

Díaz and Schmidt [2007] found that the amplitude and frequency of temperature oscillations depend on both the operating parameters and the vapor quality. The oscillations were found to increase with increasing heat flux and with decreasing mass flux. Pronounced instability in the wall temperature was observed for low qualities, oscillating at low frequencies. Amplitude was found to be greatest in the subcooled boiling region just before nucleate boiling begins. The amplitude was found to decrease significantly with increasing vapor quality. Huh et al. [2007] found that fluctuations in wall temperature were exactly out of phase with both mass flux and heat flux.

Wu and Cheng [2003] carried out a study of periodic boiling in two sets of trapezoidal microchannels, one set with a hydraulic diameter of 431 μm and one set with a hydraulic diameter of 160 μm . For the 431 μm diameter channels, the inlet water temperature fluctuated the most (amplitude $\approx 70^\circ\text{C}$) and the outlet water temperature fluctuated the least (amplitude $\approx 10^\circ\text{C}$), with the wall temperatures fluctuating somewhere in-between the two (amplitude $\approx 20\text{-}50^\circ\text{C}$). For the 160 μm diameter channels, the inlet water temperature fluctuated the most (amplitude $\approx 65^\circ\text{C}$) and the outlet water temperature did not fluctuate at all. The wall temperatures decayed along the flow direction, from about 45°C near the inlet to about 10°C near the outlet. The fluctuation period for the small channels was found

to be 141 seconds, compared to only 31 seconds for the larger channels. The boiling mode near the exit of the channel was alternating bubbly flow, elongated bubbly/slug flow, semi-annular flow, and annular/mist flow. The boiling mode in the middle of the microchannel was alternating bubbly flow, elongated bubbly/slug flow, and semi-annular flow. All of the wall temperatures and the inlet temperature oscillate in-phase due to periodic reversed flow.

Wang et al. [2007] carried out an experiment in silicon microchannels of trapezoidal cross-section and 186 μm diameter for two test sections: one with eight parallel channels and one with a single channel of the same geometry. It was found that the oscillation period of the temperature was dependant only on the heat-to-mass flux ratio and completely independent of the heat flux. However, the oscillation periods were much longer for the single channel (around 10 to 80 seconds) than those for the multiple channel test section (around 2.5 to 9.8 seconds). It is also interesting to note that the relationship between oscillation period of temperature and heat-to-mass flux ratio was linear for the parallel microchannels and parabolic for the single microchannel.

Individual bubbles have a greater effect on parameters such as pressure fluctuations in microchannels due to their small internal volume. Zhang et al. [2005] observed pressure fluctuations having the same frequency as the bubble departure frequency. These transient pressure fluctuations that are induced by bubble nucleation are significantly higher than what have been observed on a macro scale. The frequency of pressure fluctuations was found to increase with increasing

heat flux, but was independent of the mass flux for both parallel microchannels and a single microchannel [Wang et al., 2007]. The amplitude of pressure drop oscillations can be used as an index for the appearance of reversed flow [Chang and Pan, 2007].

Wu and Cheng [2003] observed that mass flux fluctuated with respect to time, having the same period as the temperature and pressure fluctuations. A phase lag occurred between the pressure drop and mass flux oscillations. Barber et al. [2008] identified three time scales apparent in the pressure and temperature measurements for flow boiling in a single rectangular microchannel of diameter 727 μm . The small amplitude/short-period fluctuations are apparently due to the dynamic bubble instabilities during two-phase flow. This finding is similar to that of Wu and Cheng [2003].

The magnitude of the temperature fluctuations at this time scale is approximately 16°C and the magnitude of the pressure fluctuation is approximately 25 mbar. The average fluctuation of the heat transfer coefficient was 500-700 $\text{W}/\text{m}^2\text{K}$. As expected, the heat transfer coefficient is at its maximum when the average temperature is at its minimum. As can be seen, the fluctuations for each of the three different time scales have smaller amplitudes for smaller periods. The existence of large amplitude/long period oscillation and small amplitude/short period oscillation has been verified by Xu et al. [2005], using the power spectral density (PSD) technique.

2.5 Influence of Nanofluids

A number of excellent review papers related to heat transfer using nanofluids have been published recently [Daungthongsuk and Wongwises, 2007; Godson, et al., 2010; Kakac and Pramuanjaroenkij, 2009; Wang and Mujumdar, 2008 a; Wang and Mujumdar, 2008 b; Wen, et al., 2009]. They show that addition of nanoparticles essentially enhances thermal conductivity of the mixture. The effective conductivity of nanofluids can be affected by mechanisms of particle motion such as dispersion of suspended particles, intensification of turbulence, Brownian motion, thermophoresis, and diffusiophoresis. Thermophoresis causes a force to be exerted on a nanoparticle in the presence of a temperature gradient; the particles travel in direction of decreasing temperature. Diffusiophoresis (osmophoresis) occurs when particles migrate from lower concentration to higher concentration. Brownian motion, thermophoresis, and diffusiophoresis are significant in the absence of turbulent eddies [Buongiorno, 2006]. When nanofluids are used in flow boiling, the nanoparticles become deposited on the surface and change its thermal conductivity, roughness, capillarity, wettability, and nucleation site density. These parameters influence bubble growth and triple line dynamics.

The addition of nanoparticles to a working fluid can significantly increase heat exchanger performance due to the non-linear increase in thermal conductivity of the nanofluid. The increase in heat transfer performance is speculatively attributed to the nanoparticle interactions with the channel walls and the surrounding fluids; the nanoparticles serve as heat carriers and collide with the channel walls, disturbing the

boundary layer and moving across the bulk fluid. This movement flattens the fluid temperature profile and increases the temperature gradient near the wall which increases the heat transfer rate [Wu et al., 2009].

Thermal resistance has been shown to be significantly lowered for single phase flow by more than 28% for log-mean temperature difference [Ho, et al., 2010]. The use of nanofluids has also been found to increase performance by reducing the fin thermal resistance [Bhattacharya, et al., 2009]. The convective heat transfer coefficient of single phase flow with nanofluids has been found to increase by as much as 70% [Ho, et al., 2010] and becomes more appreciable at higher Reynolds number [Jung, et al., 2009].

The pressure drop penalty for the addition of nanofluids has been shown to be negligible with respect to the increase in heat exchange performance. With concentrations of 0.15 vol% and 0.26 vol% alumina nanoparticles in water, pressure drop has been shown to increase by 3-4.2% and 3.4-5.5%, respectively [Wu, et al., 2009]. Although the increase in thermal conductivity enhances heat exchanger performance, the relative decrease in the specific heat of the nanofluid plays a counteracting role and can increase both fluid and wall temperatures [Lee and Mudawar, 2007].

The thermal conductivity of a nanofluid is affected by particle size, particle aspect ratio, particle composition, and fluid temperature. The relative size of the particle with respect to the roughness of the heating surface also plays an important role in understanding boiling behavior [Godson, et al., 2010]. Flow boiling CHF

enhancement has been shown to increase with mass flux and nanoparticle concentration. The maximum CHF enhancements for 0.001 vol%, 0.01 vol%, and 0.1 vol% alumina (Al_2O_3) nanofluids have been observed at 33%, 44%, and 53%, respectively [Kim, S. J., et al., 2009]. CHF enhancements of alumina nanofluids were observed by a different study to be almost unchanged within margin of error for concentrations from 0.001 vol% to 0.1 vol%; it was concluded that the effects of deposition may already be saturated at 0.001 vol% [Kim, T. I., et al., 2010]. The addition of 1% polyolester and 0.02 vol% CuO particles to R-134a has been found to have no apparent effect on heat transfer coefficient, but concentrations of 1% polyolester and 0.04 vol% or 0.08 vol% CuO increased the heat transfer coefficient by 42-82% [Henderson, et al., 2010]. A 1 vol % alumina addition to water caused catastrophic failure during two-phase flow due to the clogging of channels by nanoparticle deposition [Lee and Mudawar, 2007].

Particle composition can also have a large effect on CHF enhancement. Maximum flow boiling enhancements for alumina, zinc oxide, and diamond nanofluids were 53%, 53%, and 38%, respectively [Kim, S. J., et al., 2010]. Pool boiling CHF enhancements for alumina, zirconia, and silica nanofluids are 52%, 75%, and 80%, respectively [Kim, S. J., et al., 2007].

The boiling curve for nanofluid pool boiling has been found to be shifted to the right due to nanoparticle deposition [Xue, et al., 2007]. Nanoparticle deposition can affect nucleate boiling heat transfer coefficient via alteration of surface thermal conductivity, roughness, capillary wicking, wettability, and nucleation site density

[Kim, S. J., et al., 2010]. It can also affect heat transfer by changing bubble departure diameter, bubble departure frequency, and the evaporation of the micro and macrolayer beneath the growing bubbles [Ahn, et al., 2010]. Significant CHF enhancement has been found to occur for pure water on a nanoparticle fouled surface [Kim, H., et al., 2010]. Decrease in contact angle due to nanoparticle fouling is observed for both pure water and nanofluids after nanofluid boiling, indicating that the change was due to the surface properties and not the effects of nanoparticles in the liquid [Kim, S. J., et al., 2007].

A threefold increase in CHF has been shown to be possible for nanofluids in pool boiling [You, et al., 2003]. Results show that the key parameter to explain enhanced flow boiling CHF is the improved surface wettability due to nanoparticle deposition. The CHF data seem to be well correlated to the contact angle of the nanofluid-boiled surface regardless of flow velocity. The effects of surface modification and flow velocity have been found to be independent of each other. Ahn, Kim et al. observed CHF enhancement for a no-flow condition to be about 50%, whereas for low-flow velocities it is ~25% and at increased flow velocities it increased to ~42% [Ahn, et al., 2010].

Hypotheses for the mechanism causing CHF on a heater surface fall into four major categories: Hydrodynamic instability theory, macrolayer dryout theory, hot/dry spot theory, and bubble interaction theory. Hot/dry spot theory assumes CHF occurs when the evaporation recoil force that causes a meniscus to recede becomes larger than the surface tension force that drives the meniscus to advance

and rewet the hot/dryspot. This theory predicted an increase in CHF for a nanofluid pool boiling experiment of around 73%, which was very close to the experimental observations and could link the enhancement in CHF to the increased surface wettability [Kim, S. J., et al., 2007]. Hot/dry spot theory incorporated with the microhydrodynamics of the evaporating meniscus is a very plausible mechanism to explain the CHF enhancement in nanofluid pool boiling. The surface modification due to nanoparticle deposition has been shown to improve the stability of the evaporating meniscus enough to withstand a twofold increase in evaporation recoil force at higher superheat and heat flux [Kim, H., et al., 2010].

Effective contact angles have been observed to be reduced from 83° to 20° after nanoparticle fouling [Kim, S. J., et al., 2009]. A decrease in contact angle can decrease the active nucleation site density and reduce the heat transfer coefficient. This effect could be countered by the number of microcavities that the porous layer creates [Kim, S. J., et al., 2007]. Depending on range of cavity diameter and depth, nucleation site density ratio can range from ~ 0.7 to ~ 1.9 [Kim, S. J., et al., 2009]. Surface roughness does not show a significant effect on CHF values because the sensitivity of vapor bubble growth on active nucleation site density is very weak near peak heat flux [Ahn, et al., 2010].

Analysis of Young's equation suggests that the enhancement in wettability is a result of both an increase in adhesion tension and an increase in surface roughness. The roughness of the nanoparticle coated surface has been found to increase by twenty times that of pure water and the total area increased by five times [Kim, S. J.,

et al., 2007]. When particles are deposited on the surface, an increase in effective contact area enhances the capillarity of the surface and causes the lateral wicking of fluids into the dry region beneath a growing vapor bubble, which delays the irreversible growth of hot spots and enhances CHF. The estimated heat flux gain based on capillary liquid supply alone was found to be of the same order of magnitude as the heat flux gained by the wettability effect in a pool boiling experiment of nanofluids on a wire. The measure of capillarity for surfaces with the same apparent contact angle correlated well with experimental values of CHF increase [Kim and Kim, 2007].

Wall temperatures have been observed to decrease at heat fluxes close to CHF in pure water pool boiling on a nanoparticle fouled surface due to the temperature activation of submicrometer cavities in the porous coating or the removal of nanoparticles revealing new cavities [Kim, H., et al., 2010]. Flow boiling CHF of pure water on nanoparticle coated specimens was higher than the value of pure water on a bare surface but lower than that of the nanofluids. A significant amount of nanoparticles were detached from the surface during flow boiling of pure water; the surface roughness decreased from 1740 nm to 756 nm and the contact angle increased from $\sim 10^\circ$ to 45° [Ahn, et al., 2010]. The heat transfer to nanofluids in pool boiling with a rough heater surface increased by $\sim 70\%$, whereas a smooth heater surface caused heat transfer degradation by $\sim 45\%$ [Narayan, et al., 2007]. This shows that nanoparticle detachment during flow boiling could influence CHF.

Nanoparticle coating also affects thermal effusivity, which is a representative parameter for transient heat conduction within a heater. Higher effusivity means the heater material can allow the hot/dry spot to be dissipated more effectively [Ahn, et al., 2010]. The presence of nanoparticles also affects the burnout mode during CHF by making it more localized due to the increased wettability and mitigating the propagation of hot spots [Kim, S. J., et al., 2008].

The flow boiling heat transfer coefficient of CuO/R113 nanofluid was found to be higher than that of pure R113 refrigerant by up to 29.7%, possibly due to the enhancement of heat transfer by reduction of the boundary layer height due to the disturbance effect of nanoparticles and the formation of a molecular adsorption layer on the surface of the nanoparticles [Peng, et al., 2009]. Reversal of the heat transfer coefficient versus heat flux curve at high heat fluxes has been observed and it was conjectured that this reversal is due to the accumulation of nanoparticles on the test section surface [Kim, S. J., et al., 2010].

Heat transfer coefficients for nucleate pool boiling with nanofluids have been shown in literature to be higher, lower or unchanged from that of pure water. CHF on the other hand is always increased for even very low concentrations of nanoparticles [Henderson, et al., 2010]. These discrepancies may be attributed to poorly characterized/ reported factors such as initial surface roughness, presence of surfactants, agglomeration of particles, and surface contamination, among others. [Kim, S. J., et al., 2007].

The effect of nanoparticle suspension in the bulk liquid can thin the thermal boundary layer around the wall and cause a reduction in the number of active nucleation sites. The presence of nanofluids may also affect the cavity radius distribution function and the distribution of cavity mouth angle [Wen, 2008]. Nanoparticle suspensions in liquid have been shown to reduce bubble departure volume by 25% and increased bubble departure frequency by $\sim 1/3$ in adiabatic gas flows. This is believed to be due to a 7% reduction in surface tension by gold nanofluids. It may also be influenced by the dynamics of the triple line, such as improved wetting ability and pinning. It is likely that the changes in triple line dynamics were due to variation in the solid surface tensions and affinity for solid substrate due to the presence of nanoparticles [Vafaei and Wen, 2010]. Reduction of surface tension has been found to be as high as 50% for bismuth telluride-based nanofluids and as low as 3% for alumina nanoparticle-based nanofluids [Vafaei, et al., 2009]. Negligible particle deposition was observed for forced convection single phase flow [Wu, et al., 2009] and adiabatic two phase experiments, indicating that the change in triple line dynamics was due to particle suspension in the liquid and not through solid surface modification for the flow conditions studied in these experiments [Vafaei and Wen, 2010].

In microlayer evaporation, flow and heat transfer are coupled with the capillary force, intermolecular interactions (disjoining pressure), and fluid surface interactions (wetting phenomena). In nanofluids, a structural disjoining pressure arises due to the presence of nanoparticles suspended in the extended microlayer of

an evaporating meniscus. The extended microlayer has a thickness between one and a few nanoparticle diameters, where the wetting and dynamics of the interface are determined by the effects of evaporation, vapor recoil, capillary force, and the structural disjoining pressure. The structural disjoining pressure is a long range force that acts normal to the wall. It arises due to the ordering of particles in the confinement of the thin film region, as opposed to their greater freedom of motion in the bulk liquid. The structuring force exhibits an improved spreading capability of nanofluids in confined spaces and has been observed to change the macroscopic contact angle of a liquid droplet, stabilize liquid films, and lift an oil droplet from a wall in an aqueous solution. The enhanced spreading capability can increase the rewetting ability of a fluid in boiling [Wen, 2008].

3 Methods

The flow loop consisted of a syringe pump, an in-line heater, a microfluidic tee for liquid inlet temperature measurement, and a microchannel test section (Figure 3.1). The syringe pump provided a constant flow rate of de-gassed, de-ionized water or 0.001 vol% alumina nanofluids. After the syringe pump, the water was passed through a constant heat flux in-line resistive heater consisting of a metal tube with insulation and resistive heating wire wrapped around it in order to adjust the inlet temperature to the microchannel. A microfluidic tee was located after the in-line heater, with a 0.25 mm, type T thermocouple submersed in the flow to measure

the fluid inlet temperature (TC_1). After the microchannel test section, the water was discharged into a beaker.

The microchannel test section consisted of a single microchannel cut into a 400 micron-thick piece of brass using a micro-milling machine. The cross-section was slightly trapezoidal, with the bottom of the trench about 40 microns smaller than the top of the trench. The nominal rectangular cross-section dimensions were 266 μm deep by 201 μm wide, giving a hydraulic diameter of 229 μm . The channel was 25.4 mm long with 7 mm of uncut brass surrounding it on all sides.

A microheater was placed behind the brass with three 0.25 mm, type T thermocouples located directly underneath the channel on the brass surface, between the microheater and the brass (TC_2 , TC_3 , TC_4). Water was introduced into the microchannel through a polycarbonate face plate which was bolted in-place with a steel back plate that sandwiched the microchannel, microheater, and insulation between it and the faceplate (Figure 3.2). The thermocouple attached to the steel back plate (TC_5) was used to determine the overall heat flux into the microchannel by interpolating heat loss readings for the dry microchannel and subtracting from the overall heat input as measured by the laboratory power supply.

Before the experiment, de-ionized water was de-gassed by rapid depressurization, using the procedure reported in Steinke and Kandlikar [2004]. The procedure was repeated five times to ensure that bubble formation was due to the onset of nucleate boiling rather than degassing. Alumina nanofluids were added to the water after the degassing process so that the final concentration was 0.001

vol%. The nanoparticle suspension was manufactured by Sigma-Aldrich and purchased online from Nanostructured and Amorphous Materials, Inc. The nanoparticles are 30 nm +/- 10 nm in size and made of aluminum oxide. They come suspended in water at 20 wt% and were diluted using volumetric measurement to 0.001 vol%. The nanofluid mixture was shaken in a beaker before use to ensure that the concentration was uniform throughout the mixture. Uncertainty on the final nanofluid concentration is +/- 0.00001 vol% as calculated from manufacturer specifications.

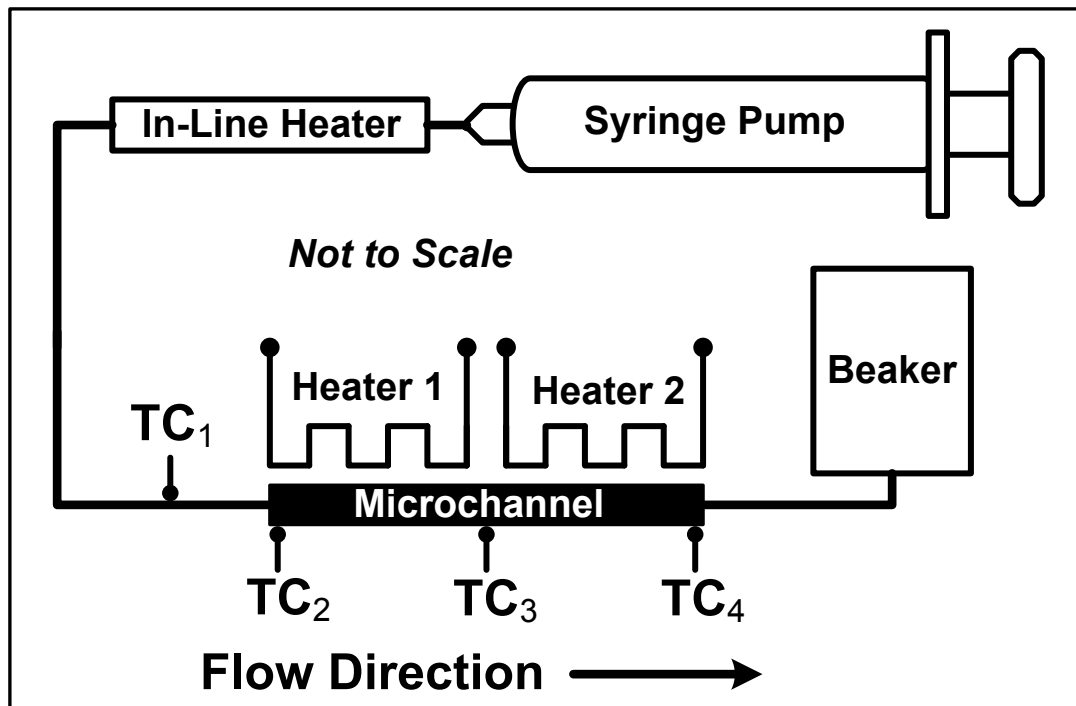


Figure 3.1: Experimental flow loop. Tests were performed at flow rates of $Re = 100$ and $Re = 200$ for different heat fluxes, corresponding to average surface temperatures of 103°C and 119°C for each flow rate. Inlet fluid temperature was held at a constant $63^{\circ}\text{C} \pm 1^{\circ}\text{C}$ for all test conditions. [Edel and Mukherjee, 2012]

The syringe pump was operated at two constant flow rates of 0.41 ml/min and 0.82 ml/min, which corresponds to liquid Reynolds numbers of 100 and 200 using the saturation temperature of water at atmospheric pressure. The power input to the in-line heater was adjusted so that the inlet temperature was a constant $63^{\circ}\text{C} \pm 1.0^{\circ}\text{C}$. The power input to the microchannel was adjusted so that the average surface temperature was a constant 103°C or 119°C over the duration of water and nanofluid flow boiling. Data were taken during the transient process of nanoparticle deposition and flow boiling over a total duration of 160 minutes for each nanofluid flow boiling case. Measurements were taken for water after 60 minutes of flow boiling.

Conditions were considered to be at steady state when the temperature measured by the thermocouple on the outside of the test section (TC_5) was constant for a full ten minutes; this generally occurred after about 20 min of running the experiment due to the thermal mass of the test section. A fiber-optic cold light source illuminated the microchannel and high speed video was recorded at 10,000 fps over the downstream half of the microchannel at flow boiling durations of 25, 75, and 125 minutes after the start of flow. Temperature readings were taken every 100 ms using a laboratory data acquisition system and averaged over 1 second intervals.

Channel width and height were measured using an interferometric microscope. Uncertainty on channel width was approximately $\pm 24 \mu\text{m}$; uncertainty on channel depth was approximately $\pm 1.7 \mu\text{m}$. Bottom surface roughness was approximately $0.1 \mu\text{m}$. Experimental uncertainty for the thermocouple measurements is

approximately $\pm 1^\circ\text{C}$ on an absolute temperature scale, and $\pm 0.1^\circ\text{C}$ thermocouple-to-thermocouple. Temperatures have been reported to 1°C accuracy.

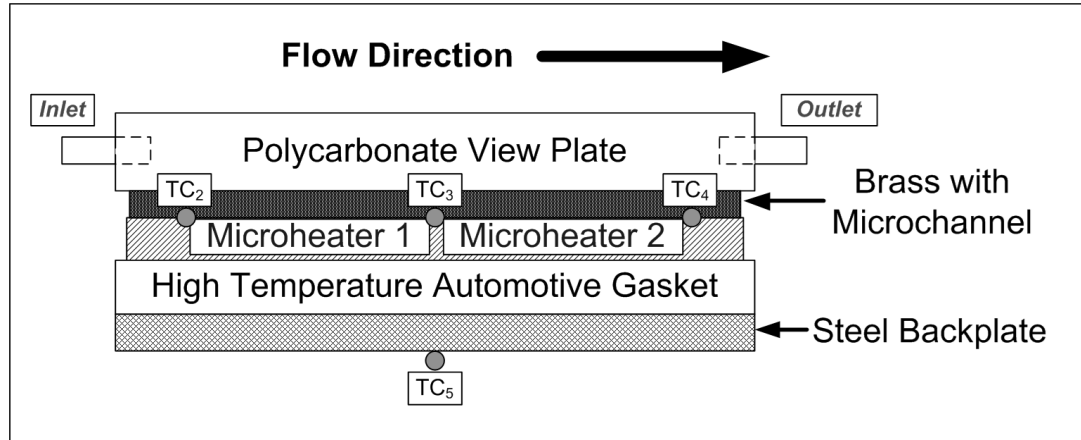


Figure 3.2: Schematic of the test section. Thermocouples were placed at three locations under the brass microchannel and at one location on the back of the test section assembly. [Edel and Mukherjee, 2012]

4 Results and Discussion

4.1 Location of the Onset of Bubble Elongation (OBE)

For an average surface temperature of 105°C , an inlet temperature of 64°C , and a Reynolds number of 200 an upstream progression of bubble elongation was visible (see Figure 4.1.1). The bubbles would slide along the wall and travel downstream at a speed close to the liquid flow rate. As the local surface temperature increased in time, the bubbles would grow faster and eventually the Onset of Bubble Elongation (OBE) would be reached before the bubbles exited the microchannel.

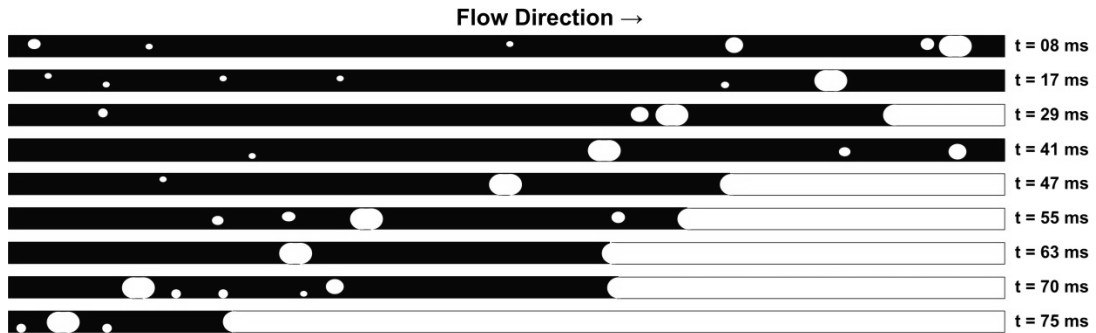


Figure 4.1.1: Images of the upstream progression of the Onset of Bubble Elongation (OBE) for water at $Re = 200$, $T_{s,avg} = 105^{\circ}C$, $T_{in} = 64^{\circ}C$. Black indicates liquid and white indicates vapor in the microchannel. Bubbles started elongating near the channel outlet after the bubbly flow regime transitioned to bubble-slug flow. After the bubbles start evacuating the microchannel the location of OBE moves further and further upstream. [Edel and Mukherjee, 2011]

Once a bubble started to elongate near the exit of the channel, it would slow the flow of liquid or possibly even reverse the flow of liquid, causing the higher temperature liquid to reside in the microchannel for a longer period of time. This created a progression of OBE that would start near the channel exit and slowly move further and further upstream.

Figure 4.1.2 shows a measurement of OBE location versus time from the start of the elongation sequence at the channel exit (distance from inlet = 25 mm). Bubbles started elongating near the exit and then began to elongate further and further upstream as time progressed. Two different progression rates can be seen in Figure 4.1.2; one that corresponds to a flow regime oscillation pattern of liquid/two-phase/vapor and one that corresponds to an oscillation pattern of two-phase/vapor.

The different rates of progression in this case indicate the effects of conjugate heat transfer from the stationary thermal mass of the test section to the fluid in the microchannel. As the flow alternated from vapor back to liquid, two different flow patterns were observed. In the first flow pattern, the channel would flood with liquid and slowly change to two-phase flow as the liquid in the channel was heated past the saturation temperature (see Figure 4.1.3). The flow would eventually become annular and then dry out. In the second flow pattern, two-phase flow would start occurring before the liquid phase could fully flood the microchannel and would continue until annular flow and dryout were reached (see Figure 4.1.4).

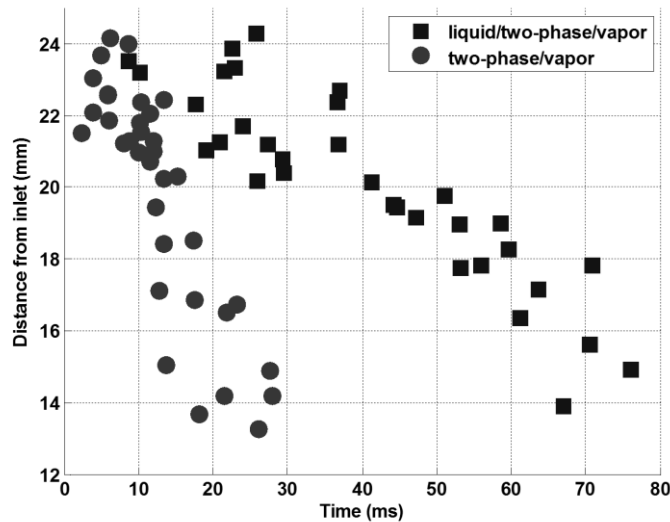


Figure 4.1.2: Location of OBE versus time for water at $Re = 200$, $T_{s,avg} = 105^{\circ}C$, $T_{in} = 64^{\circ}C$. For the liquid/two-phase/vapor flow regime transition pattern the location of OBE moved upstream at a slower progression rate than for the two-phase/vapor flow regime transition pattern. [Edel and Mukherjee, 2011]

In the first case, the liquid was allowed to dissipate the temperature of the sidewalls before the OBE sequence started, creating a lower instantaneous surface temperature and a lower progression rate. In the second case, the channel walls did not have time to cool down before the start of OBE. The higher instantaneous surface temperature caused an increased rate of progression of OBE in the upstream direction.

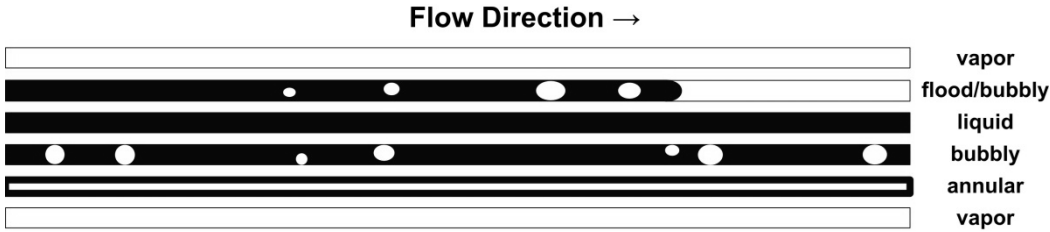


Figure 4.1.3: Liquid/two-phase/vapor flow pattern. Black indicates liquid and white indicates vapor in the microchannel. Liquid appears exclusively in the microchannel before bubbly flow transitions to vapor. [Edel and Mukherjee, 2011]

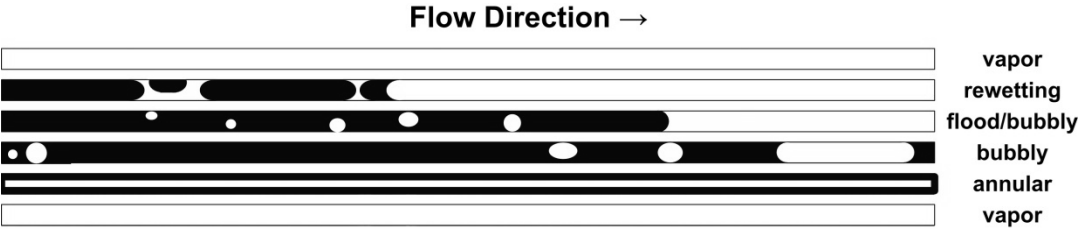


Figure 4.1.4: Two-phase/vapor flow pattern. Black indicates liquid and white indicates vapor in the microchannel. The bubbly flow regime appears before the microchannel can completely flood and the flow regime transitions from bubbly to annular without the appearance of single-phase liquid in the entire viewing window. [Edel and Mukherjee, 2011]

Records of the location of OBE for water and after different durations of nanofluid flow boiling are given in Figure 4.1.5 at different flow rates and surface temperatures. For $Re = 100$ and $T_s = 103^\circ\text{C}$ the distributions of OBE are somewhat irregular for water and become more repeatable with the addition of nanoparticles.

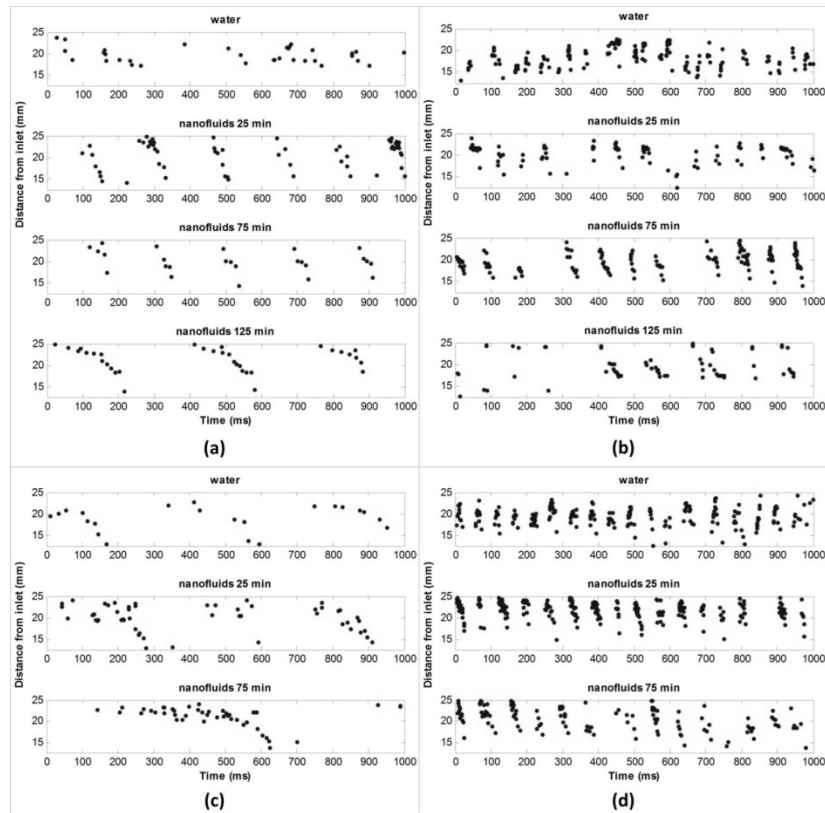


Figure 4.1.5: Records for the location of OBE as measured from the inlet for (a) $Re = 100$, $T_s = 103^\circ\text{C}$, (b) $Re = 100$, $T_s = 119^\circ\text{C}$, (c) $Re = 200$, $T_s = 103^\circ\text{C}$, (d) $Re = 200$, $T_s = 119^\circ\text{C}$. The progression of OBE location occurs less rapidly as nanoparticles deposit on the microchannel surface. This is seen for both flow rates at the lower surface temperature. When the flow rate was increased from $Re = 100$ to $Re = 200$ the progression rate occurred less rapidly for the lower average surface temperature.

OBE regularity increases with surface temperature, flow rate, and nanofluid flow boiling duration for all cases. Flow regime transition occurs more rapidly at higher wall surface temperatures for both flow rates. The duration of a typical flow regime transition cycle increases drastically with flow rate at $T_s = 103^\circ\text{C}$, whereas the duration decreases slightly with flow rate at $T_s = 119^\circ\text{C}$. The behavior of flow transition at different surface temperatures changes with flow rate due to the effect of nucleation site availability on the upstream progression rate of OBE. A higher frequency of ONB causes the progression of OBE location to occur faster at higher surface temperatures, changing the overall length of the flow transition cycle. For a flow rate of $Re = 100$, the progression of OBE location occurs slower with the deposition of nanoparticles due to a decrease in the progression rate of the upstream interface as lateral wicking of liquid into the thin film regions increased thin film evaporation. The overall duration of two-phase flow is highest with respect to overall cycle duration at the highest flow rate of $Re = 200$ and the lowest surface temperature of $T_s = 103^\circ\text{C}$. This case exhibits the slowest progression rate of OBE location.

Figure 4.1.6 shows histograms for the location of OBE with respect to the channel inlet for water and after different durations of nanofluid flow boiling for different flow rates and surface temperatures. The normality of OBE distribution increases with an increase in channel surface temperature for both flow rates. The distribution of OBE location tends to spread out and centralize toward the downstream end of the microchannel with nanofluid flow boiling for all cases. The

spreading out of the distribution represents a more stable flow regime transition cycle due to the regularity of surface temperature oscillations.

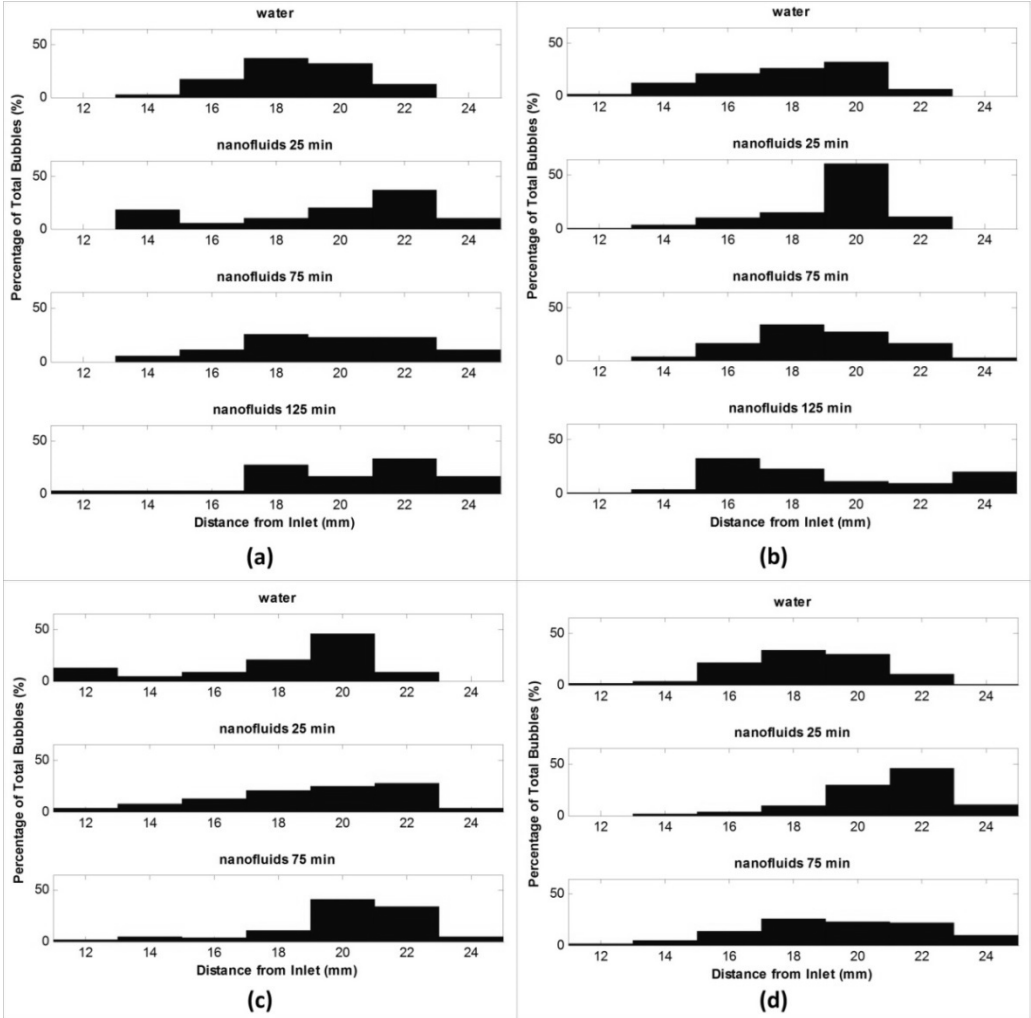


Figure 4.1.6: Histograms for the location of OBE as measured from the inlet for (a) $Re = 100$, $T_s = 103^\circ\text{C}$, (b) $Re = 100$, $T_s = 119^\circ\text{C}$, (c) $Re = 200$, $T_s = 103^\circ\text{C}$, (d) $Re = 200$, $T_s = 119^\circ\text{C}$. The location of OBE tended to spread out as nanoparticles deposited on the microchannel surface. The histograms centralized further downstream as nanofluid flow boiling continued.

The distributions tend to centralize near the downstream end of the microchannel due to the higher liquid temperatures in this region. These histograms are indicative of stabilized bubble growth with respect to instantaneous local surface temperature at the channel walls.

4.2 Bubble Growth Rates

As heat flux increases, the number of bubbles that simultaneously nucleate on the channel walls increases. These bubbles disrupt flow and create local pressure spikes that can influence the growth of adjacent bubbles. Bubble interaction depends on local fluid temperatures and pressures, proximity of nucleation sites to each other and to the inlet and outlet plenums, and upstream and downstream flow compressibility.

Figure 4.2.1 (a) depicts an example of interaction effects between two growing vapor bubbles. Flow is in the right-to-left direction, as indicated by the arrow. In this image sequence, the rapid growth of an elongating vapor bubble suppresses the growth of a nearby vapor bubble that has not yet reached the channel diameter. Both bubbles continuously increase in size from $t = 0$ ms until $t = 3.67$ ms, when the larger bubble reaches the channel diameter. At this point the smaller bubble is 143 μm in size. The larger bubble then rapidly expands and causes the smaller bubble to contract from $t = 3.67$ ms until $t = 6.67$ ms, when it reaches a minimum size of 112 μm . The smaller bubble then begins to grow again from $t = 6.67$ ms until $t = 8.00$ ms, when the two bubbles merge into one large vapor slug.

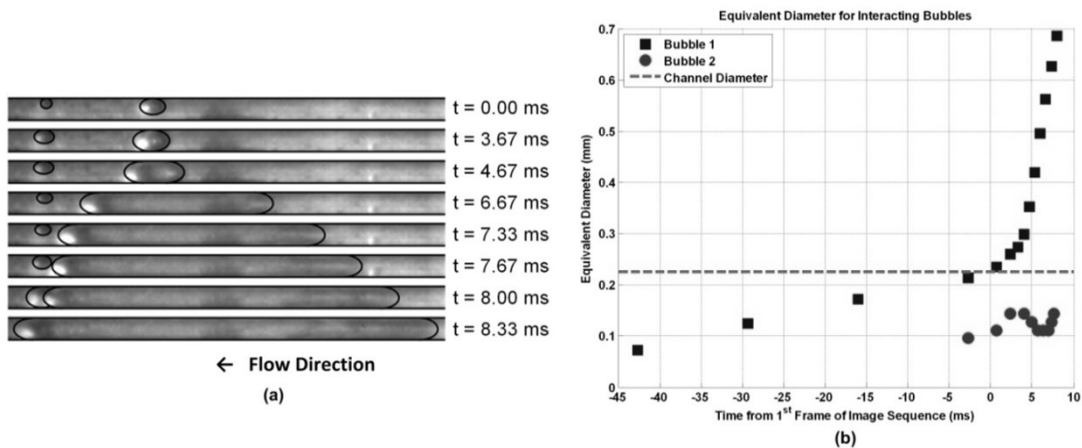


Figure 4.2.1: Bubble growth rates for water; (a) Image sequence of bubble interaction, (b) equivalent diameter of interacting bubbles. The growth of one vapor bubble is suppressed by the elongation of a neighboring vapor slug.

Figure 4.2.1 (b) shows the equivalent diameter of each bubble from Figure 4.2.1 (a), from the time that the larger bubble is less than half the channel diameter until the time when the two bubbles merge. The equivalent diameter is calculated assuming a sphere of equal volume. Bubble 1 grows linearly with time until it reaches the channel diameter, represented by a dotted line. The bubble then begins to elongate and trap thin films of liquid around the vapor core that are subject to high thermal gradients. The thin film evaporation creates an explosion of vapor pressure that causes the larger bubble to grow exponentially and induces a spike in local pressure which causes the smaller bubble to compress. The smaller bubble decreases in size until the thermal boundary layer that surrounds the larger bubble is pushed into it, increasing the local fluid temperature and causing it to grow again.

The smaller bubble continues to grow until the liquid-vapor interfaces meet and the bubbles merge.

Figure 4.2.2 shows the equivalent diameter of several elongated vapor bubbles under the same flow rate ($Re = 200$) and inlet fluid temperature (80°C) for three different values of wall surface temperature.

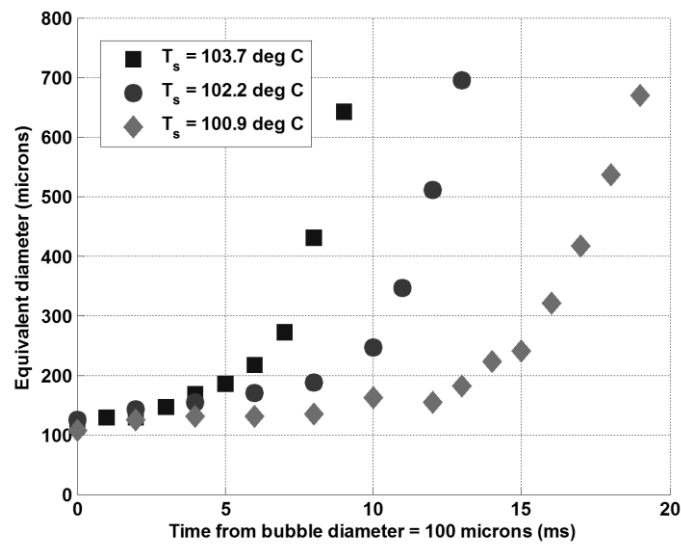


Figure 4.2.2: Bubble growth rates for water at different surface temperatures and $T_{in} = 80^\circ\text{C}$, $Re = 200$. Bubble growth rate increases with average surface temperature and becomes exponential after OBE for all temperatures. The microchannel hydraulic diameter is $229 \mu\text{m}$. [Edel and Mukherjee, 2011]

The equivalent diameter was calculated assuming a sphere of equal volume. The bubble growth was measured during the time period from when the bubbles were half the channel diameter until they were about four times longer than the channel diameter. The bubble growth curves are aligned so that at time $t = 0 \text{ ms}$

each bubble is approximately 100 μm in diameter. These bubbles were determined to be due to the Onset of Nucleate Boiling (ONB) and not dissolved gas since the fluid was de-gassed before the experiment.

For a local surface temperature of 100.9°C, it took approximately 19 ms for a bubble to grow from 100 μm in diameter to about 700 μm equivalent diameter. When local surface temperature was increased to 102.2°C, it took approximately 13 ms to reach this size. When local surface temperature was increased further to 103.7°C, it took only 9 ms for the bubble to reach this size.

As wall superheat was increased, the temperature gradient in the thin films surrounding the vapor core also increased. Increased vapor generation from the higher heat flux through the thin film regions forced the upstream and downstream interfaces away from the bubble center and elongated the thin film regions. Elongation of the thin films increased the surface area of the liquid vapor interface, thereby adding to the vapor generation rate and causing the bubbles to grow faster. Bubble growth was somewhat linear for the early stages of growth, before the bubbles reached the channel diameter, and then became exponential as the bubbles started to elongate and trap thin films between the heated wall and vapor core.

The effect of mass flux on bubble growth is depicted in Figure 4.2.3. These bubbles were measured at Reynolds numbers of 100 and 200 for an inlet temperature of 80°C and an average surface temperature of 102°C.

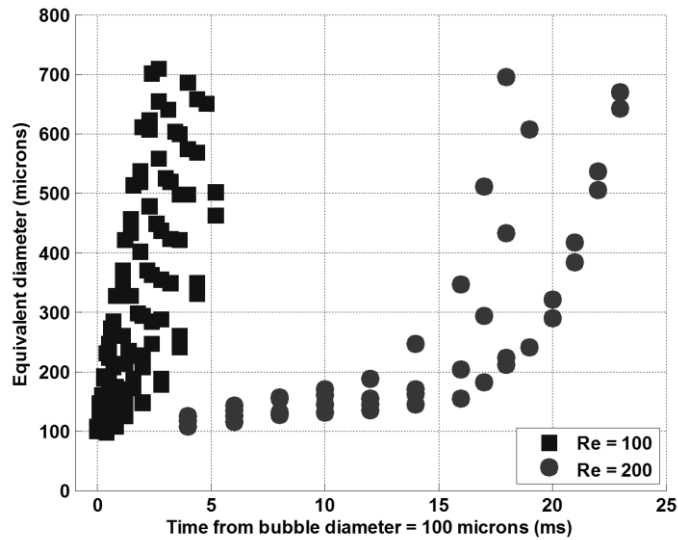


Figure 4.2.3: Bubble growth rates for water at different mass fluxes and $T_{in} = 80^{\circ}\text{C}$, $T_{s,avg} = 102^{\circ}\text{C}$. Bubble growth rate was slower for $Re = 200$ than for $Re = 100$ before OBE. Growth rates become exponential after OBE for both flow rates. Microchannel hydraulic diameter is $229\ \mu\text{m}$. [Edel and Mukherjee, 2011]

The bubble growth rates differ the most for the time period before the bubble reaches the channel diameter. For the higher flow rate, the mass flux causes the thermal boundary layer at the wall to be thinner, exposing the bubble to lower liquid temperatures in the faster flowing center of the microchannel. The increased flow drag also pushes the bubbles further downstream and sweeps them away from the sidewalls. After the bubbles reach the channel diameter, thin film evaporation begins to dominate the effect of incoming mass flux and the bubbles grow at very similar rates regardless of mass flux.

The thin film lengths for the three bubbles depicted in Figure 4.2.2 are shown in Figure 4.2.4 (a) for comparison to the corresponding bubble length. The reported film length is the combined length of the upstream and downstream thin film regions. It can be seen from Figure 4.2.4 (a) that the thin films do indeed elongate as the bubble grows, and that they maintain a combined length that is about half of the overall bubble length. This relationship may vary depending on the coolant type, channel material, and surface characteristics of the microchannel.

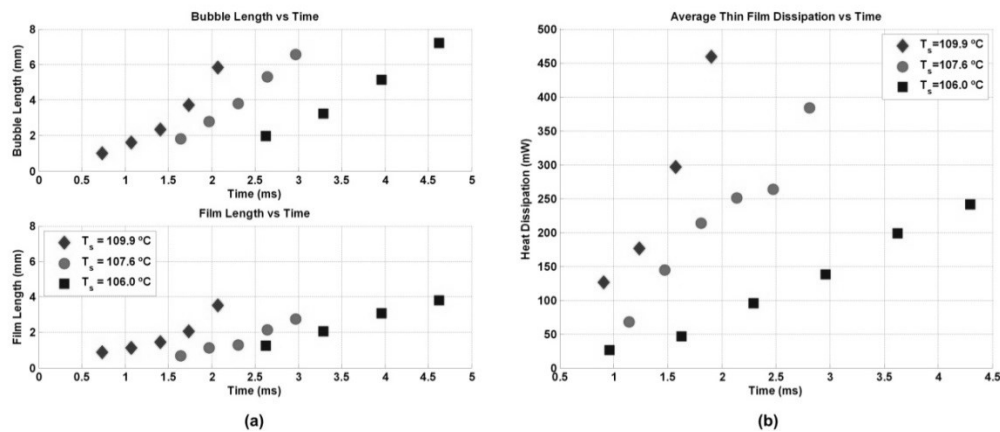


Figure 4.2.4: Bubble lengths and thin film dissipation for water; (a) Comparison of combined thin film length to overall bubble length, (b) average thin film latent heat dissipation for three values of wall surface temperature. The thin films elongate with interface recession. The amount of heat dissipated in the thin film regions increases with slug growth.

The average thin film latent heat dissipation for the three cases shown in Figure 4.2.4 (a) was calculated by measuring the volume change of the vapor in the microchannel over time and is reported in Figure 4.2.4 (b). Thin film evaporation

was assumed to be the dominant heat transfer mechanism since both the upstream and downstream interfaces quickly receded from the nucleation site after the bubble reached the channel diameter. As can be seen, the average thin film heat dissipation increases with increasing surface temperature. The rate of heat removal also increases as the thin films become longer. Although the thin films grow to approximately the same length for all three cases, the maximum heat dissipation is much higher for increased surface temperatures due to a theoretically larger temperature gradient across the thickness of the thin films.

Figure 4.2.5 shows the bubble growth measurements for water on a clean surface at $Re = 100$, $T_{in} = 68^{\circ}C$, and $q'' = 260 \text{ kW/m}^2$. The upper plot shows the bubble measurements with respect to the beginning of the cycle, whereas the bottom plot shows the bubble measurements with respect to the time at which each bubble is half the size of the channel diameter. By comparing the order of bubbles, it can be seen that there is no definite correlation between bubble order and growth rate for water on a clean surface after the first bubble.

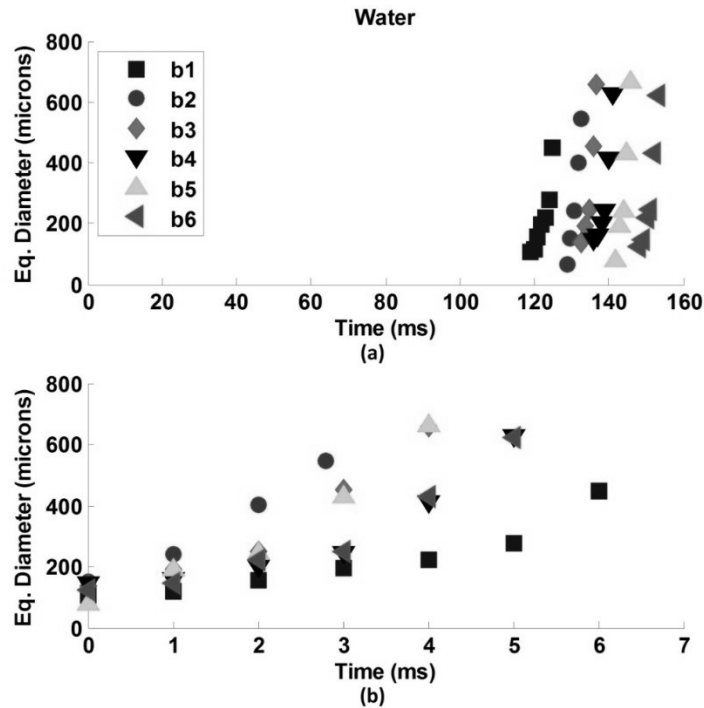


Figure 4.2.5: Bubble growth measurements for water on a clean surface at $Re = 100$, $T_{in} = 68^{\circ}C$, and $q'' = 260 kW/m^2$ with times aligned to 0 ms for (a) the start of channel flooding and (b) the time at which the bubble diameter is half that of the microchannel. The legend shows bubble order in the given cycle. The growth rate of each bubble is not dependent on bubble order. [Edel and Mukherjee, 2012]

Figure 4.2.6 shows the bubble growth measurements after 125 minutes of nanofluid flow boiling. The earliest bubbles grow the slowest and the later bubbles grow increasingly faster. The first bubbles that appear form near the channel exit. The subsequent bubbles form further and further upstream as time advances. Due to the negative temperature gradient present along the visible half of the microchannel length, the bubbles that form further from the exit experience higher local surface

temperatures and grow at a consistently increasing rate. Since this is not as visible at lesser deposition times, it is evident that the effect of the deposited nanoparticles stabilized the bubble growth rate with respect to local surface temperature.

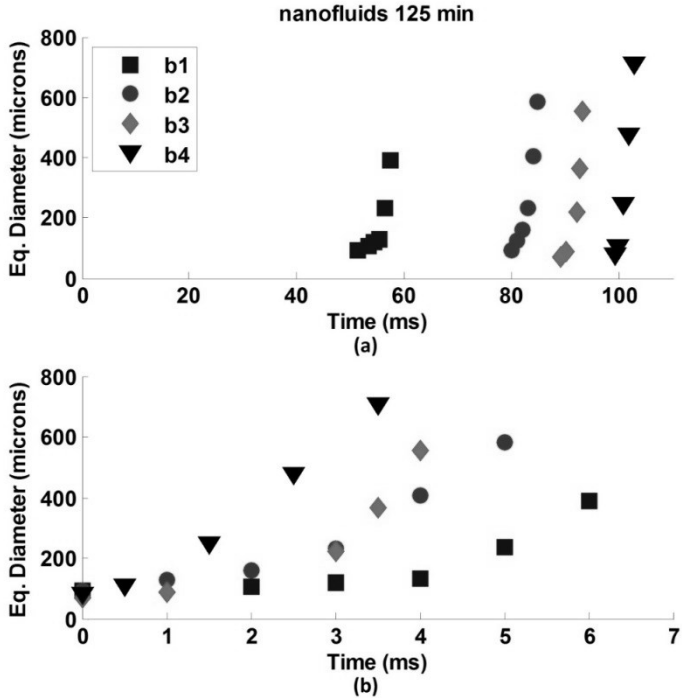


Figure 4.2.6: Bubble growth measurements after 125 minutes of nanofluid flow boiling at $Re = 100$, $T_{in} = 68^{\circ}C$, and $q'' = 260 kW/m^2$ with times aligned to 0 ms for (a) the start of channel flooding and (b) the time at which the bubble diameter is half that of the microchannel. Bubbles grow slower early in the flow cycle and faster as time progresses. [Edel and Mukherjee, 2012]

4.3 Flow Regime Transition Cycle Images

After steady state operation was reached for $Re = 100$ and $T_s = 103^{\circ}C$, water would flood the microchannel, heat up, and boil over the downstream end of the microchannel, which was observed with the high speed camera. For water on a

clean surface, bubbles would appear at nucleation sites distributed over the downstream end of the channel (Fig. 4.3.1 a). There was very little evidence of a repeatable trend as far as nucleation location is concerned in the axial direction; in other words, bubbles would form wherever the local surface temperature exceeded the minimum nucleation temperature and several nucleation sites would stay active due to advantageous surface properties such as surface roughness or cavities. The same progression of OBE was observed as was reported in Edel and Mukherjee [2011]. Bubbles started nucleating in the liquid before the microchannel fully flooded and the appearance of vapor in most of the visible channel length was observed during two-phase flow. A single flow cycle was not distinct and flooding would occur unexpectedly during the flow regime transition cycle.

After 25 minutes of nanofluid flow boiling, the nanoparticles that deposited on the channel surface increased the nucleation site density and caused the location of bubble growth to be much more consistent and repeatable cycle-to-cycle (Fig. 4.3.1 b). The microchannel completely flooded before bubble growth began and the microchannel was mostly full of liquid during two-phase flow. The bubbles would nucleate first near the exit where the liquid was hottest. As the liquid continued to heat up, the nucleation sites moved more and more upstream in a consistent pattern and the cycle would repeat after the subsequent dryout and flooding.

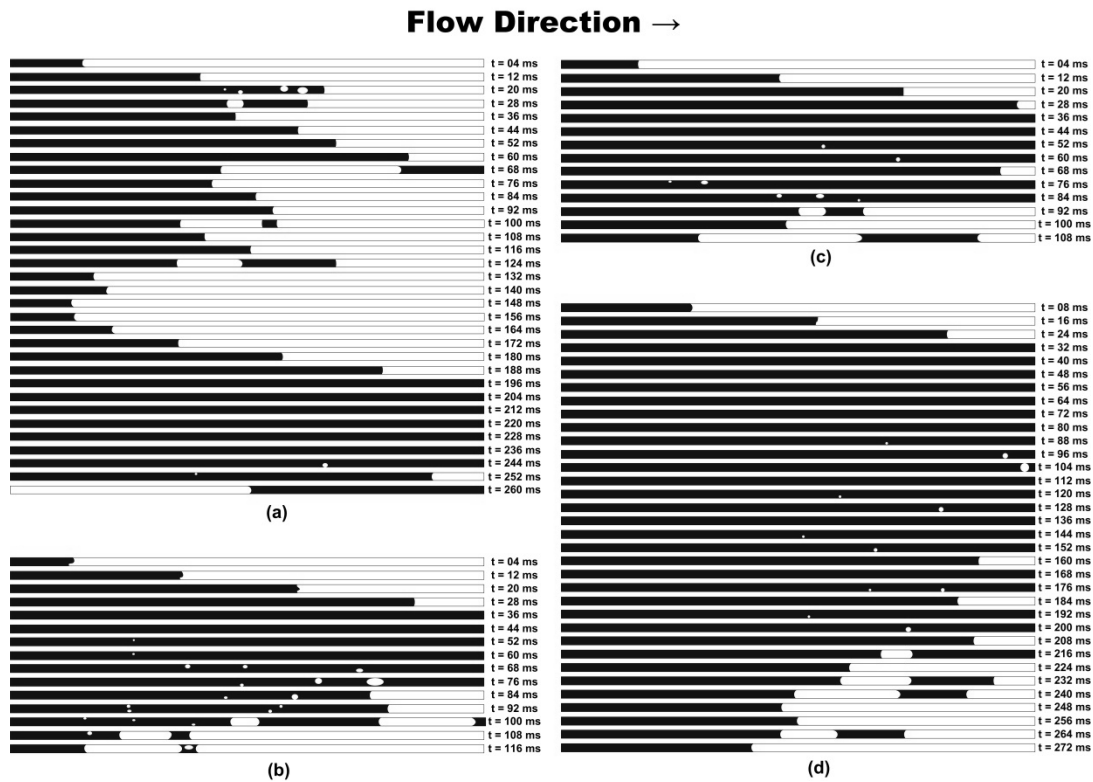


Figure 4.3.1: Image sequences for $Re = 100$, $T_{in} = 63^{\circ}C$, and $T_s = 103^{\circ}C$ for (a) water on a clean surface, and after (b) 25 minutes of nanofluid flow boiling, (c) 75 minutes of nanofluid flow boiling, and (d) 125 minutes of nanofluid flow boiling. Black indicates liquid and white indicates vapor in the microchannel. Liquid occupied a larger region of the microchannel length as nanofluid flow boiling continued, indicating a slower rise in surface temperature during a given flow cycle. [Edel and Mukherjee, 2013]

The same pattern of bubbles nucleating downstream and then progressing upstream was observed for nanofluid flow boiling after 75 minutes of operation (Fig. 4.3.1 c). However, the active nucleation sites caused OBE to progress upstream faster and less bubbles formed per flow regime transition cycle. The cycles would repeat regularly as with the case of 25 minutes nanofluid flow boiling

duration. In other words, the channel would flood, ONB would occur, and OBE would progress from channel exit to inlet before channel dryout.

The flow regime transition cycle was significantly elongated after 125 minutes of nanofluid flow boiling (see Fig. 4.3.1 d). The channel would completely flood before bubble growth, as before, and the progression of OBE occurred from exit to inlet, as before. However, the progression of OBE occurred much slower than in the previous cases, indicating an increase in mass transfer into the thin film regions of the evaporating meniscus. More liquid appears in the image sequence because the thin film evaporation at the upstream interface would dissipate heat faster and cause less of the bulk fluid to evaporate over channel length. An increase in the liquid appearing in the microchannel indicates a slower increase in local surface temperature due to the dissipation of the bulk liquid during two-phase flow.

Figure 4.3.2 (a) shows a typical flow transition cycle at $Re = 100$ and $T_s = 119^\circ\text{C}$ for water on a clean surface. ONB occurs almost immediately after the channel starts to flood and the constant elongation of bubbles prevents the channel from completely flooding at any time during the flow transition cycle. The upstream interface takes on different shapes for this case, with the behavior approaching annular flow near the end of the liquid phase in the microchannel before $t = 9.0$ ms. After $t = 9.0$ ms, the rate at which evaporation cools the microchannel surface has decreased the local surface temperature enough to support a typical microlayer evaporation scenario and caused the interface to take on a spherical shape, as with $Re = 100$ and $T_s = 103^\circ\text{C}$.

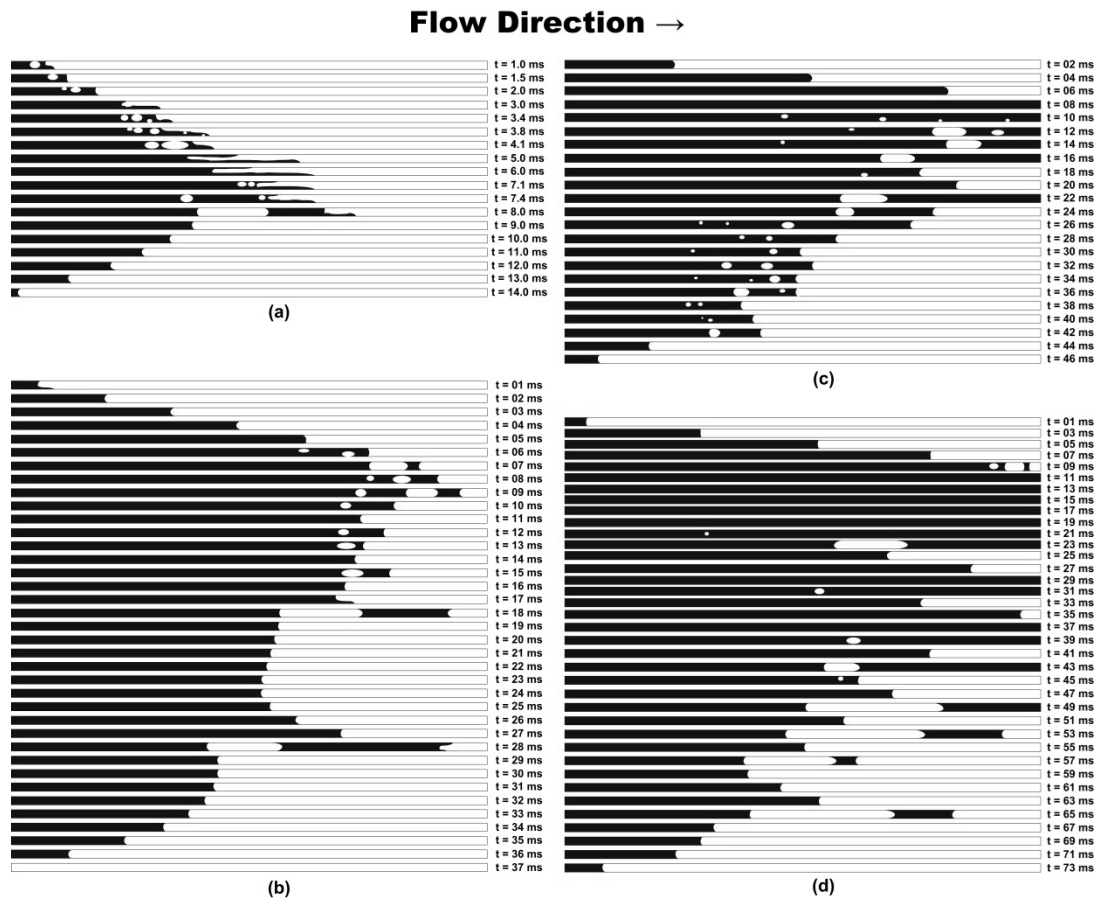


Figure 4.3.2: Image sequences for $Re = 100$, $T_{in} = 63^{\circ}C$, and $T_s = 119^{\circ}C$ for (a) water on a clean surface, and after (b) 25 minutes of nanofluid flow boiling, (c) 75 minutes of nanofluid flow boiling, and (d) 125 minutes of nanofluid flow boiling. Black indicates liquid and white indicates vapor in the microchannel. The microchannel does not fully flood for water on a clean surface. After 125 minutes of nanofluid flow boiling the microchannel fully floods with liquid before OBE occurs.

[Edel and Mukherjee, 2013]

The rate at which the upstream interface evaporates eventually exceeds the liquid flow rate and the upstream interface recedes beyond the upstream end of the view window, leading to channel dryout. The change in the shape of the interface in

this case is indicative of a decrease in local surface temperature during two-phase flow while the liquid is evaporating near the upstream interface. Once the channel cooled enough, a typical shaped microlayer appeared and the annular flow behavior was attenuated.

The flow regime transition cycle was significantly elongated after 25 minutes of nanofluid flow boiling at $Re = 100$, $T_s = 119^\circ\text{C}$ (Fig. 4.3.2 b). The microchannel is flooded past the center point of the visible section of the microchannel before ONB occurs for this case, indicating that the instantaneous local surface temperature is lower during the period of channel flooding. ONB occurs before the microchannel is completely flooded and the shape of the upstream interface is spherical for almost all cases, indicating that the increase in surface wettability and capillarity due to nanoparticle deposition enhances the wicking of liquid into the microlayer region of the evaporating meniscus and cools the microchannel more effectively. One appearance of semi-annular flow occurs at $t = 28$ ms when an upstream vapor bubble causes the liquid velocity at the downstream end of the liquid slug to exceed the rate at which a typical microlayer can dissipate liquid and the shape of the liquid-vapor interface takes on a perturbed shape as for the case of water on a clean surface.

After 75 minutes of nanofluid flow boiling, the channel completely floods before ONB occurs (Fig. 4.3.2 c). OBE takes place from channel exit to inlet as was seen with nanofluid flow boiling at $Re = 100$ and $T_s = 103^\circ\text{C}$. The flow regime transition cycle is elongated from 37 ms of two-phase flow to 46 ms of two-phase

flow. More microbubbles are observed in the liquid phase, indicating an increase in nucleation site density on the channel surface with the deposition of nanoparticles. The upstream interface takes on a spherical shape for all images shown, which indicates superior cooling ability of the evaporating meniscus during two-phase flow.

Figure 4.3.2 (d) shows a typical flow regime transition cycle after 125 minutes of nanofluid flow boiling at $Re = 100$ and $T_s = 119^\circ\text{C}$. ONB occurs before the channel is completely flooded, but then stops as cool liquid is pushed over the heated surface and decreases the superheat of available nucleation cavities. ONB starts again at $t = 21$ ms when the progression of OBE continues from exit to inlet until channel dryout. The two-phase portion of the cycle is elongated from 46 ms to 73 ms. Less bubbles are observed to form, which indicates that the evaporation heat transfer is more efficient due to the increased mass flux of liquid into the thin film region. The increased amount of water seen in the image sequences after nanofluid flow boiling is also indicative of increased mass flux into the thin film regions during two-phase flow. There is less liquid visible in the image sequences for $T_s = 119^\circ\text{C}$ than for $T_s = 103^\circ\text{C}$ because the higher surface temperatures evaporate the liquid earlier in the flow cycle for the higher heat flux.

A typical flow transition cycle for $Re = 200$ and $T_s = 103^\circ\text{C}$ is shown in Figure 4.3.3 (a) thru (c) for water on a clean surface and after 25 minutes and 75 minutes of nanofluid flow boiling, respectively.

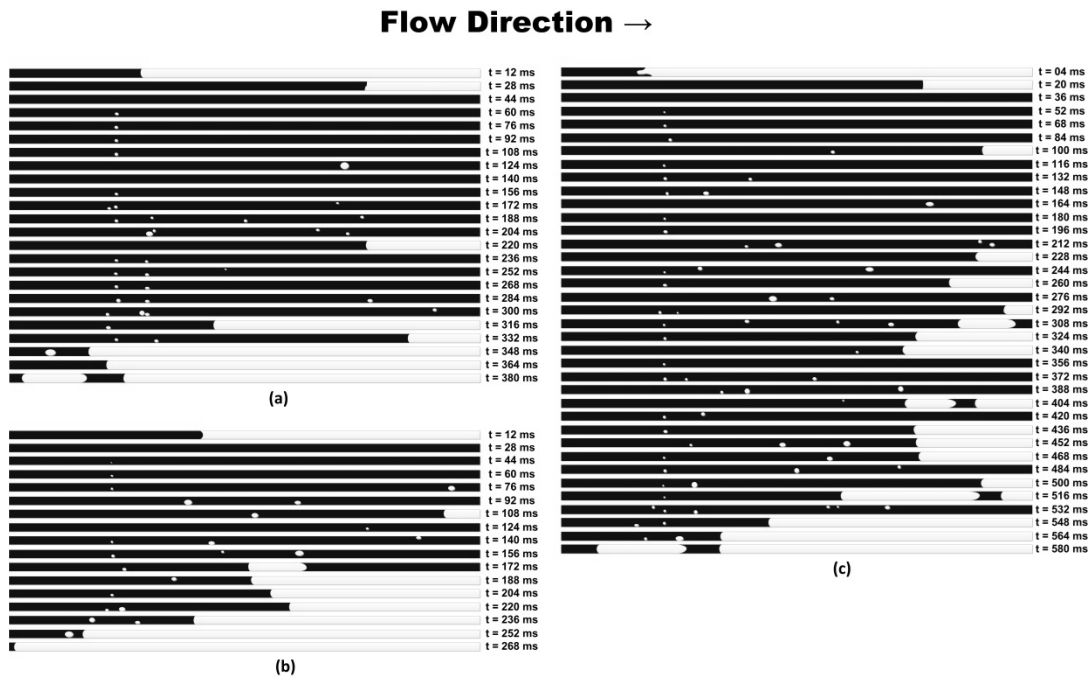


Figure 4.3.3: Image sequences for $Re = 200$, $T_{in} = 63^{\circ}C$, and $T_s = 103^{\circ}C$ for (a) water on a clean surface, and after (b) 25 minutes of nanofluid flow boiling, and (c) 75 minutes of nanofluid flow boiling. Black indicates liquid and white indicates vapor in the microchannel. The upstream interface moves toward the inlet at a slower pace after 125 minutes of nanofluid flow boiling.

Liquid completely wets the surfaces before ONB for all cases. The complete wetting of the microchannel for water represents a stabilization of flow with an increase in flow rate while maintaining the same average surface temperature as for Figure 4.3.1. The increased nucleation site density after 75 minutes of nanofluid flow boiling causes more bubbles to form and grow per cycle, which decreases instantaneous surface temperature and increases the duration of two-phase flow with respect to channel dryout and overall cycle length. The increased duration of two-

phase flow represents a more stable flow transition cycle when nanoparticles are added to the flow.

Typical flow regime transition cycles at $Re = 200$ and $T_s = 119^\circ\text{C}$ are shown in Figure 4.3.4 (a) thru (c) for water on a clean surface and after 25 minutes and 75 minutes of nanofluid flow boiling, respectively. Bubbles start to nucleate and elongate before the channel completely floods for all cases. The higher surface temperature with respect to the previous case causes the upstream interface to start receding during the flooding period for water, as seen in Figure 4.3.2 (a) at $t = 03$ ms. The interface profile is convex rather than concave for this flow rate and surface temperature due to the high rate of evaporation at the channel surfaces. The cooling of the channel walls by evaporation eventually dominates the evaporation process at $t = 05$ ms to the point of where the interface profile straightens out and the channel continues to flood. ONB and OBE occur during channel flooding and causes the channel to dryout after $t = 21$ ms. The addition of nanoparticles in parts (b) and (c) stabilizes the surface temperatures enough to eliminate the initial interface recession during flooding and causes ONB and OBE to occur more regularly as the liquid enters the microchannel. The increased nucleation site density causes more bubbles to form and grow per cycle, decreasing the instantaneous channel surface temperature and increasing the duration of two-phase flow with respect to overall cycle duration.

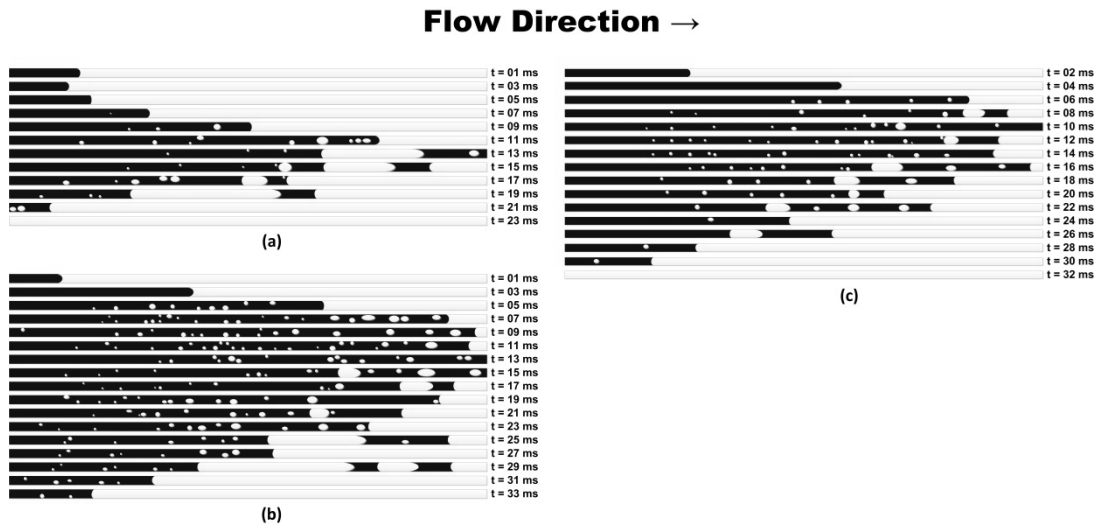


Figure 4.3.4: Image sequences for $Re = 200$, $T_{in} = 63^{\circ}C$, and $T_s = 119^{\circ}C$ for (a) water on a clean surface, and after (b) 25 minutes of nanofluid flow boiling, and (c) 75 minutes of nanofluid flow boiling. Black indicates liquid and white indicates vapor in the microchannel. The upstream interface moves toward the inlet at a slower pace after 125 minutes of nanofluid flow boiling.

4.4 Phase Records

A record of the phases appearing at the channel outlet is given in Figure 4.4.1 (a) thru (d) for water on a clean surface and for different durations of nanofluid flow boiling at $Re = 100$ and $T_s = 103^{\circ}C$. A value of one represents single phase vapor appearing at the outlet and a value of zero represents single phase liquid appearing at the outlet.

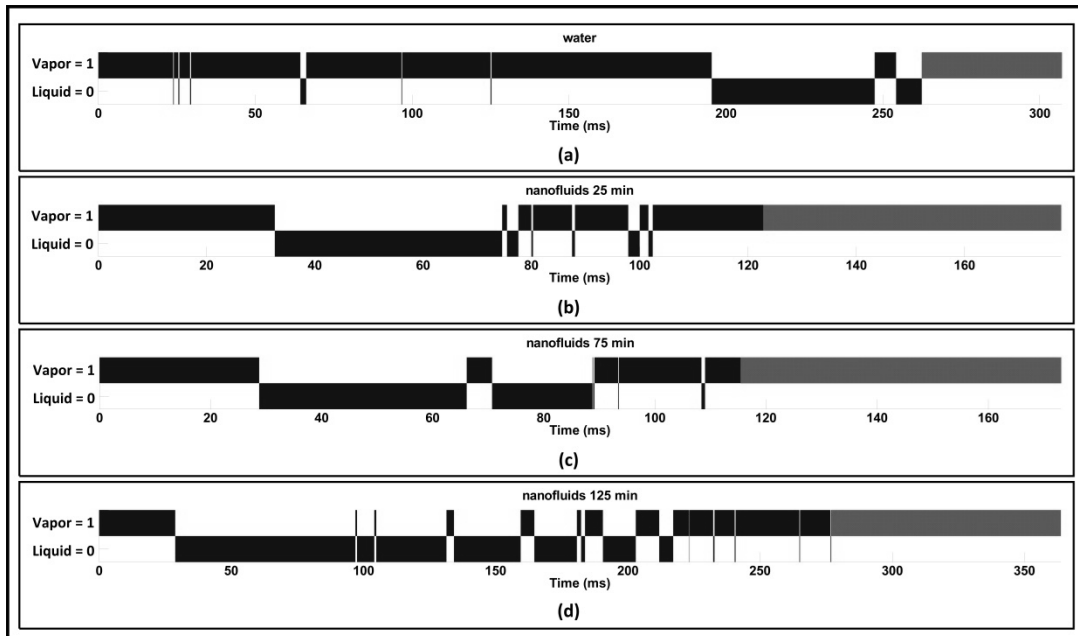


Figure 4.4.1: Liquid/Vapor phase record of single phase flow at the channel outlet for $Re = 100$, $T_{in} = 63^{\circ}C$, and $T_s = 103^{\circ}C$ for (a) water (b) nanofluids 25 minutes, (c) nanofluids 75 minutes, and (d) nanofluids 125 minutes. The black line indicates two-phase flow and the grey line indicates channel dryout. Two-phase flow persists over a greater percentage of the flow cycle as nanoparticles deposit on the microchannel surface. [Edel and Mukherjee, 2013]

The dark line starts when flooding occurs and there is a delay before ONB, OBE, and liquid appearing at the channel outlet. The diagrams end in grey, which signifies the time that the downstream end of the microchannel is fully dried out. Each plot is scaled so that one flow regime transition cycle is the same length in the figure. The scaling allows the portions of the flow cycle to be compared in terms of the percentage of total cycle length rather than actual duration in milliseconds. The cycle shown is characteristic for the flow regimes.

The amount of time that the channel is dried out initially increases and then decreases with nanofluid flow boiling. After 125 minutes duration the amount of time the channel dries out is still higher for nanofluids than for water. The duration of two phase flow oscillation at the outlet, shown as the duration over which the line is changing from zero to one or vice versa, initially decreases when nanofluids are added to the flow. This duration then increases with nanofluid flow boiling from 25 minutes to 125 minutes duration. The total amount of liquid leaving the channel outlet continually increased with flow boiling duration. A larger amount of liquid appearing at the outlet signifies a slower rise in local wall temperature during two phase flow. Slower instantaneous surface temperature rise during two-phase flow is indicative of a higher evaporative heat transfer coefficient at the upstream interface due to the increased mass transfer into the thin film regions introduced by the enhanced capillarity from nanoparticle deposition. After 75 minutes of nanofluid flow boiling, the duration of channel dryout begins to decrease due to enhanced thin film evaporation.

Figure 4.4.2 (a) thru (d) shows the phase records for water and different flow boiling durations at $Re = 100$ and $T_s = 119^\circ\text{C}$. For water on a clean surface, almost no liquid appears at the exit due to the high surface temperatures with respect to the flow rate. The overall duration of two-phase flow increases with nanoparticle deposition as seen before, indicating more efficient cooling of the channel walls during two-phase flow.

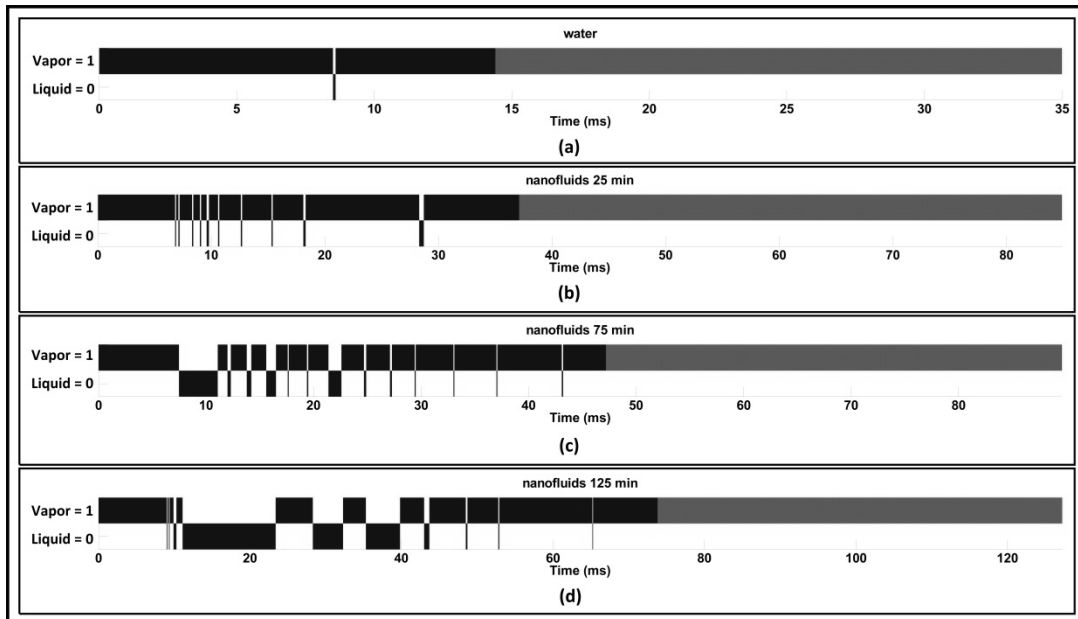


Figure 4.4.2: Liquid/Vapor phase record of single phase flow at the channel outlet for $Re = 100$, $T_{in} = 63^{\circ}\text{C}$, and $T_s = 119^{\circ}\text{C}$ for (a) water (b) nanofluids 25 minutes, (c) nanofluids 75 minutes, and (d) nanofluids 125 minutes. The black line indicates two-phase flow and the grey line indicates channel dryout. Single-phase vapor occupies the microchannel for a smaller percentage of the flow cycle as nanofluid flow boiling continues. [Edel and Mukherjee, 2013]

Individual durations of liquid flow at the outlet increase with time in one cycle due to surface temperature increase, as before. It takes longer for liquid flow to appear at the outlet for the case of $Re = 100$ and $T_s = 119^{\circ}\text{C}$ than it did for the case of $Re = 100$ and $T_s = 103^{\circ}\text{C}$. The duration of dryout continually decreases with nanofluid flow boiling.

The phase record for water and different durations of nanofluid flow boiling at $Re = 200$ and $T_s = 103^{\circ}\text{C}$ is shown in Figure 4.4.3 (a) thru (d). The overall

durations of two-phase flow for this case are longer than for the previous cases of lower flow rate. The durations of dryout are shorter for this case as well.

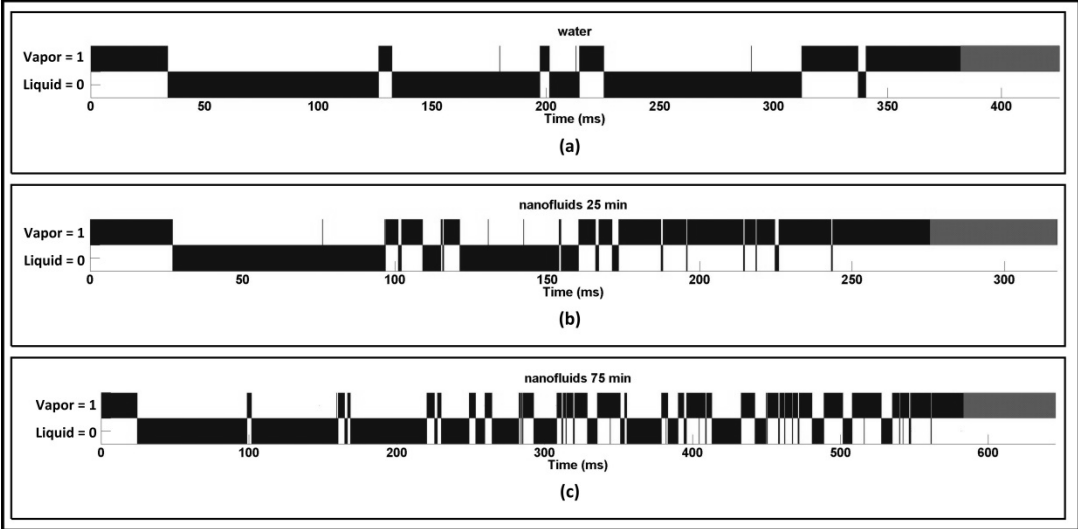


Figure 4.4.3: Liquid/Vapor phase record of single phase flow at the channel outlet for $Re = 200$, $T_{in} = 63^{\circ}C$, and $T_s = 103^{\circ}C$ for (a) water (b) nanofluids 25 minutes, and (c) nanofluids 75 minutes. The black line indicates two-phase flow and the grey line indicates channel dryout. The flow oscillates more rapidly between single-phase liquid and single-phase vapor at the outlet after 75 minutes of nanofluid flow boiling.

The overall length of two-phase flow increases with nanoparticle deposition as before. The duration of dryout decreases after only 25 minutes of nanofluid flow boiling duration for this case, which is shorter than the previous cases at 75 minutes duration. Liquid flow at the outlet appears much earlier in the cycles than for the previous cases with lower flow rates.

Figure 4.4.4 (a) thru (c) shows the phase records for $Re = 200$ and $T_s = 119^{\circ}C$. The overall duration of two-phase flow for water is higher for this case than for the

case of $Re = 100$ and $T_s = 103^\circ\text{C}$. The phases at the outlet oscillate between liquid and vapor much more rapidly for this case than for previous cases of lower flow rate and/or surface temperatures.

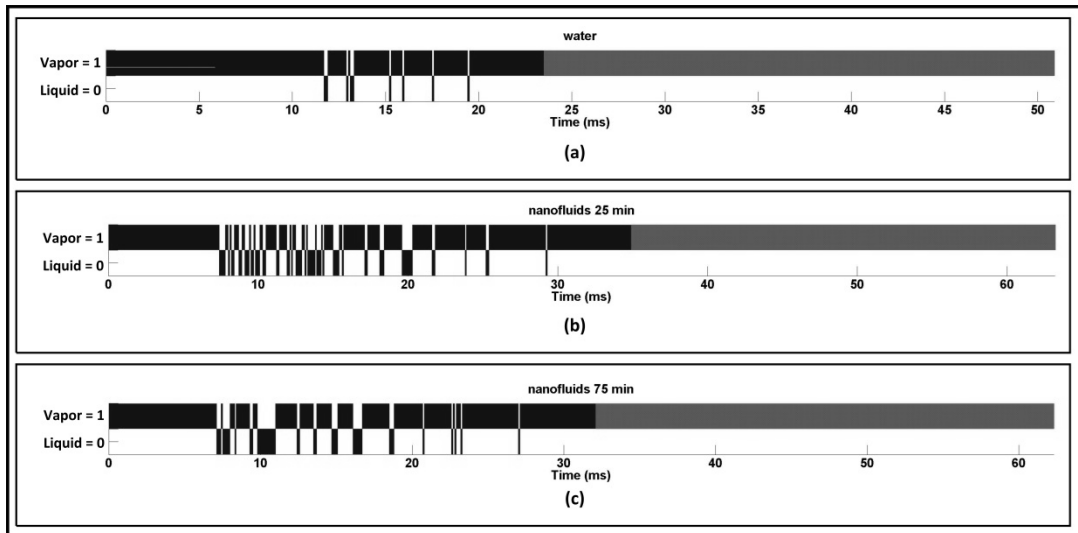


Figure 4.4.4: Liquid/Vapor phase record of single phase flow at the channel outlet for $Re = 200$, $T_{in} = 63^\circ\text{C}$, and $T_s = 119^\circ\text{C}$ for (a) water (b) nanofluids 25 minutes, and (c) nanofluids 75 minutes. The black line indicates two-phase flow and the grey line indicates channel dryout. Two-phase flow occupies the microchannel for a smaller percentage of the flow cycle when flow rate and surface temperature are increased as compared to previous trials.

The duration of channel dryout initially decreases for 25 minutes nanofluid flow boiling duration and then increases at 75 minutes duration. The total duration of dryout for this case is shorter after 75 minutes of nanofluid flow boiling than it is for water. The overall length of channel dryout is higher for this case than for previous cases.

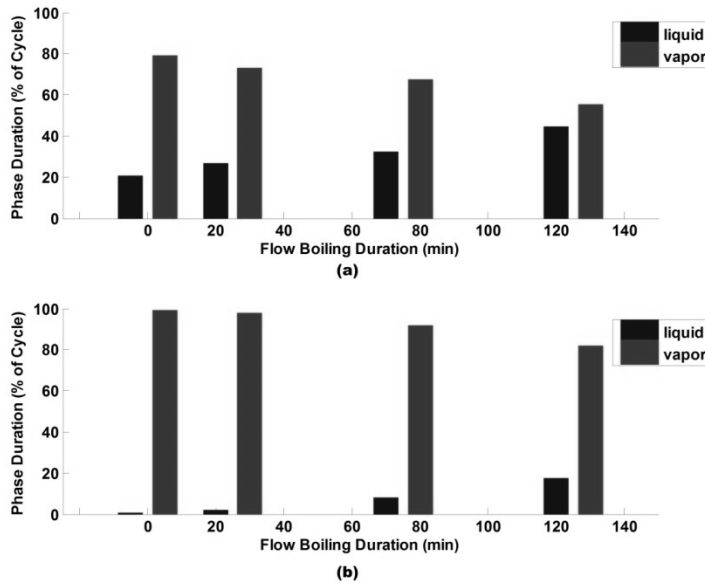


Figure 4.4.5: Percentage of flow cycle occupied by single phase flow for $Re = 100$ and (a) $T_s = 103^\circ\text{C}$ and (b) $T_s = 119^\circ\text{C}$ as a function of nanofluid flow boiling duration. The flow boiling duration of zero corresponds to water flow boiling on a clean surface. More liquid appears at the microchannel outlet as nanofluid flow boiling continues due to the slower rise in surface temperatures during two-phase flow.

The total durations of liquid and vapor flow at the channel outlet are given in Figure 4.4.5 in terms of the percentage of the total cycle duration for $Re = 100$ and different surface temperatures. The duration of liquid flow at the outlet continually increases with nanofluid flow boiling duration for both cases. More liquid appears at the outlet for $T_s = 103^\circ\text{C}$ than for $T_s = 119^\circ\text{C}$ for all durations. The increase in the appearance of liquid at the outlet with nanoparticle deposition is indicative of more efficient evaporative cooling at the channel walls during two-phase flow.

4.5 Cycle Duration and Bubble Frequencies

The average duration of each flow transition cycle for water (duration = 0 min) and after different durations of nanofluid flow boiling is shown in Figure 4.5.1 at different flow rates and average surface temperature. At the average surface temperature of $T_s = 103^\circ\text{C}$, the cycle duration initially decreases with the addition of nanoparticles due to the effect of increased nucleation site density on the upstream progression rate of OBE location. For the higher surface temperature of $T_s = 119^\circ\text{C}$, the cycle duration continually increases with the addition of nanoparticles due to a slower rise in surface temperatures as increased wicking of liquids into the thin film regions of the evaporating menisci increases thin film evaporative cooling. The cycle duration ends at a higher value for nanofluid flow boiling than for water in all cases. Increased cycle duration is accompanied by an increase in two-phase flow duration with respect to overall cycle duration in all cases.

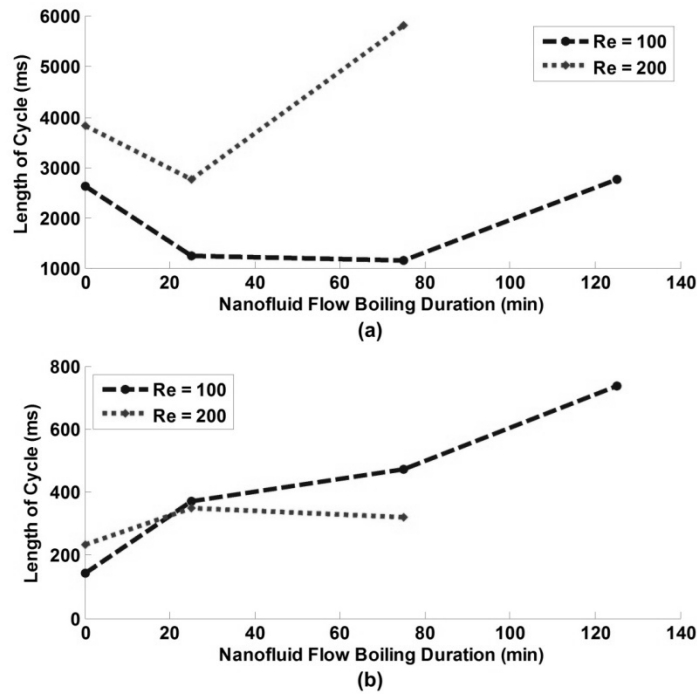


Figure 4.5.1: Length of flow regime transition cycle at different mass flow rates using water (0 min) and nanofluids for (a) $T_s = 103^\circ\text{C}$, and (b) $T_s = 119^\circ\text{C}$. The duration of the flow regime transition cycle increases with nanofluid flow boiling duration due to a slower rise in surface temperatures during two-phase flow.

The frequency of ONB is given in Figure 4.5.2 at different values of surface temperature and flow rate for water on a clean surface and after different durations of nanofluid flow boiling. For the lower surface temperature of 103°C , both ONB frequency and OBE frequency initially increase with the addition of nanoparticles due to an increase in nucleation site density. The frequencies then decrease with nanofluid flow boiling duration due to the enhanced cooling effect of thin film

evaporation on the rate of surface temperature increase due to enhanced wicking of liquids along the microchannel surface.

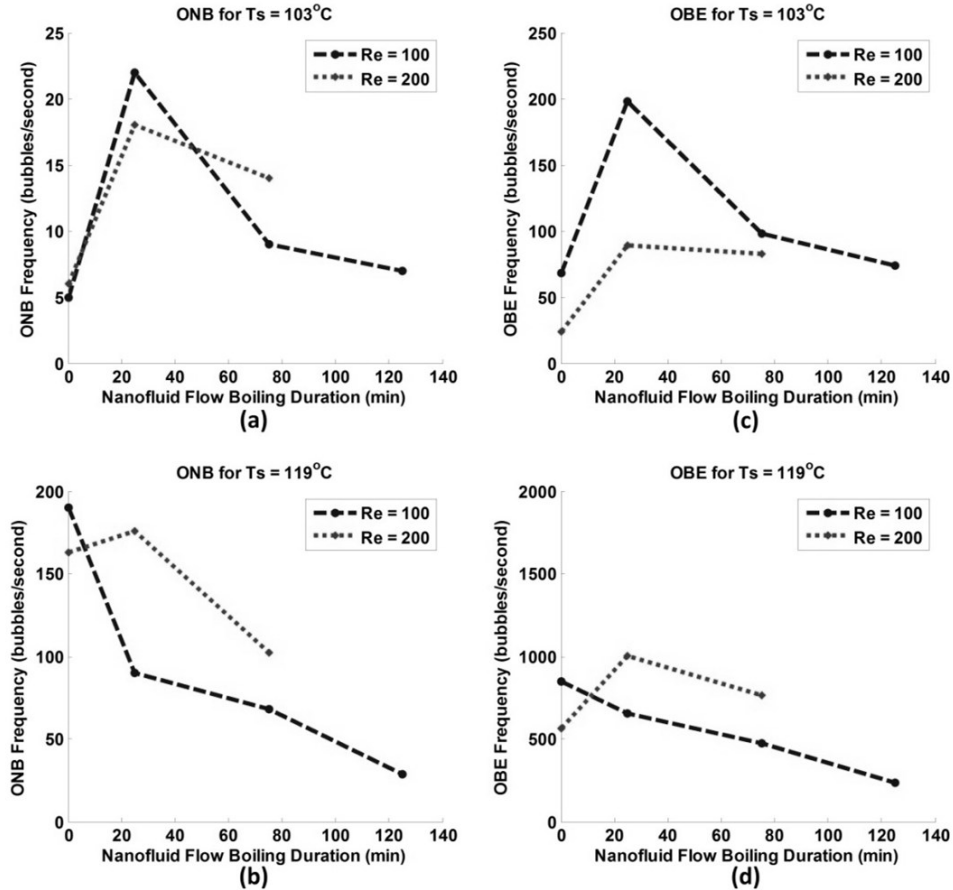


Figure 4.5.2: Bubble frequency at different average surface temperatures with water (0 min) and nanofluids for (a) ONB frequency at Ts = 103°C, (b) OBE frequency at Ts = 103°C, (c) ONB frequency at Ts = 119°C, and (d) OBE frequency at Ts = 119°C. The frequency of ONB decreases as nanofluid flow boiling continues because the deposition of nanoparticles causes a slower procession rate of the upstream interface and cools the microchannel surface more effectively.

The frequency of ONB and OBE continually decrease for $Re = 100$ and $T_s = 119^\circ\text{C}$ because the effect of nanoparticle deposition on nucleation site density is already saturated for the higher surface temperature and the effect of lateral wicking on thin film evaporation dominates the propagation rate of OBE location in the upstream direction. For $Re = 200$ and $T_s = 119^\circ\text{C}$ the effect of increased mass flow rate suppresses ONB and the initial increase in ONB and OBE frequency is again visible when nanoparticles are added to the flow. After 25 minutes, the frequencies again decrease due to enhanced thin film evaporation as nanoparticles deposit on the microchannel surface.

4.6 Future Work

For a nanofluid concentration of 0.01 vol% alumina Nanofluids, the progression of OBE location in the upstream direction periodically stopped at one main location along the microchannel length and the bubbles continually elongated near that site, at approximately 18 mm from the channel inlet (see Figure 4.6.1). The centralization of OBE location at one point in the microchannel indicates that channel dryout could effectively be mitigated when the microchannel length is half full of liquid and half full of vapor. Adding Nanofluids to a multiple microchannel test section with a concentration of 0.01 vol% alumina Nanofluids will stabilize channel-to-channel instability and should mitigate the periodic dryout of microchannels due to the effect of lateral surface wicking on interface stability.

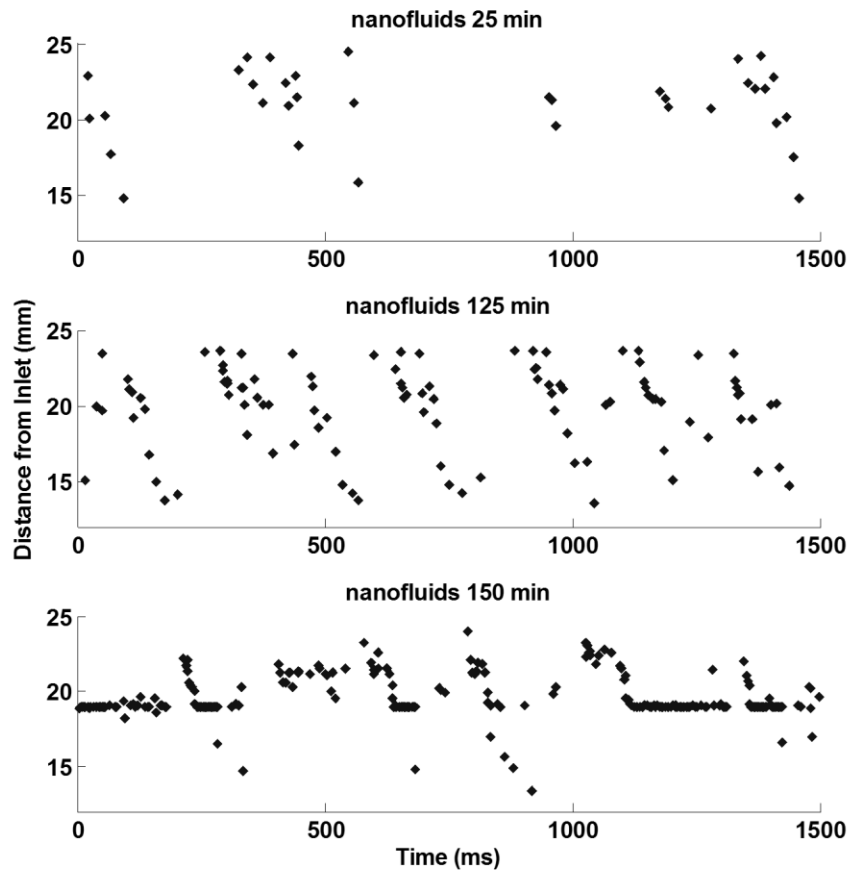


Figure 4.6.1: Records for the location of OBE as measured from the inlet for $Re = 100$, $T_s = 103^\circ\text{C}$, and a nanofluid concentration of 0.01 vol%. After 150 minutes of nanofluid flow boiling OBE location tended to centralize at 18 mm from the channel inlet.

This could lead to a spreading out of the range over which OBE occurs similar to the results from this study for a Reynolds number of 200 and an average surface temperature of 119°C . Both the mitigation of channel dryout and the spreading out of the evaporating menisci over the microchannel length will lead to more constant

heat flux footprints for micro-heat exchangers and reduce the local formation of hotspots.

In the future, I would like to stay in the area and pursue the research with the goals of integrating two-phase cooling in microchannels into a micro-processor motherboard fabricated with microchannels in the back side for stacking in a 3-dimensional microprocessor architecture. With the expansion of motherboard fabrication into a stacked architecture, the number of transistors in one core and the number of registers in one core can be increased 100 fold without having to paralyze code for multiple cores and take up more room in the computer tower. Furthermore, the 3-D microprocessor cores would be able to be integrated into a larger multi-core setup that utilizes multiple core processing with more powerful cores. The number of microchannels should be adjusted so that stable interface evaporation can be achieved in all or most microchannels in a micro heat exchanger. The length to diameter aspect ratio should be high enough to allow two-phase flow to occur over the majority of the micro heat exchanger surface. Increasing computer capability and efficiency using two-phase flow will lead to a smaller carbon footprint for data centers and will open new doors to numerical modeling on multi-scale models.

5 Conclusions

Flow boiling was investigated in this study using degassed, deionized water, and 0.001 vol% aluminum oxide nanofluids in a single rectangular brass microchannel with a hydraulic diameter of 229 μm for one inlet fluid temperature of 63°C and two constant flow rates of 0.41 ml/min and 0.82 ml/min. The power input was adjusted for two average surface temperatures of 103°C and 119°C at each flow rate. High speed images were taken periodically for water and nanofluid flow boiling after durations of 25, 75, and 125 minutes from the start of flow.

The microchannel test section consisted of a single microchannel cut into a 400 micron-thick piece of brass using a micro-milling machine. The nominal rectangular cross-section dimensions were 266 μm deep by 201 μm wide, giving a hydraulic diameter of 229 μm . The channel was 25.4 mm long with 7 mm of uncut brass surrounding it on all sides. The following conclusions can be drawn from the current study:

- The progression of the location of OBE in the upstream direction occurs more slowly for a flow regime transition cycle of liquid/two-phase/vapor than for a flow regime transition cycle of two-phase/vapor.
- The progression of the location of OBE in the upstream direction occurs more slowly for lower surface temperatures and higher flow rates.

- The deposition of nanoparticles on the microchannel surface causes the range in the location of OBE to spread out over microchannel length and centralize downstream.
- Bubbles grow more rapidly with increased surface temperature and decreased flow rate. Bubble growth rate becomes more repeatable with respect to local surface temperatures as nanoparticles deposit on the microchannel surface.
- The flow regime transition cycle changes from two-phase/vapor to liquid/two-phase/vapor with the addition of nanoparticles for $Re = 100$ because the enhanced surface capillarity due to surface modifications causes the microchannel wall surface temperature to increase less rapidly during each flow cycle.
- The increase in nucleation site density as nanoparticles deposit on the microchannel surface has the greatest effect on flow boiling stability at lower surface temperatures, where the effect of temperature on nucleation site density is not already saturated by a high excess temperature and microcavity availability is critical to the nucleation of microbubbles.
- A decrease in the duration of channel dryout with the deposition of nanoparticles is clearly visible for $Re = 100$ and $T_s = 119^\circ\text{C}$ because the slower rise in surface temperature due to enhanced thin film evaporation has a greater effect on cycle duration and the frequency of ONB.
- For an alumina nanoparticle concentration of 0.01 vol% the location of OBE tended to centralize at one location along the microchannel length, indicating

that the deposition of nanoparticles stabilizes flow regime transition and causes the visible portion of the microchannel to be half full of liquid and half full of vapor.

- The use of nanofluids to stabilize flow boiling in microchannels can mitigate channel dryout and thereby attenuate the oscillation of surface temperatures that causes the overall footprint temperature of the microchannel heat exchanger to soar.

6 References

Ahn, H. S., et al., Experimental study of critical heat flux enhancement during forced convective flow boiling of nanofluid on a short heated surface. *International Journal of Multiphase Flow*, 2010. 36(5): 375-384.

Barber, J., et al., Hydrodynamics and heat transfer during flow boiling instabilities in a single microchannel. *Applied Thermal Engineering*, 2009. 29(7): 1299-1308.

Bhattacharya, P., A. Samanta, and S. Chakraborty, Numerical study of conjugate heat transfer in rectangular microchannel heat sink with Al₂O₃/H₂O nanofluid. *Heat and Mass Transfer*, 2009. 45(10): 1323-1333.

Bruus, H., *Theoretical microfluidics*. Oxford master series in physics, 18. 2008, Oxford University Press.

- Buongiorno, J., Convective Transport in Nanofluids. *Journal of Heat Transfer*, 2006. 128(3): 240-250.
- Chamarthy, P., et al., Visualization of Convection Patterns Near an Evaporating Meniscus using Micro-PIV. *Experiments in Fluids*, 2008. 44: 431-438.
- Chang, K.H. and C. Pan, Two-phase flow instability for boiling in a microchannel heat sink. *International Journal of Heat and Mass Transfer*, 2007. 50(11-12): 2078-2088.
- Choi, S. U. S. Enhancing thermal conductivity of fluids with nanoparticles. 1995. San Francisco, CA, USA: ASME.
- DasGupta, S., I. Y. Kim, and J. P. C. Wayner, Use of the Kelvin-Clapeyron Equation to Model an Evaporating Curved Microfilm. *Journal of Heat Transfer*, 1994. 116(4): 1007-1015.
- Dasgupta, S., J. A. Schonberg, and P.C. Wayner, Investigation of an evaporating extended meniscus based on the augmented Young-Laplace Equation. *Journal of Heat Transfer – Transactions of the ASME*, 1993. 115(1): 201-208.
- Derjaguin, B., A theory of capillary condensation in the pores of sorbents and of other capillary phenomena taking into account the disjoining action of polymolecular liquid films. *Progress in Surface Science*, 1992. 40(1-4): 46-61.

- Diaz, M.C. and J. Schmidt, Experimental investigation of transient boiling heat transfer in microchannels. *International Journal of Heat and Fluid Flow*, 2007. 28(1): 95-102.
- Duangthongsuk, W. and S. Wongwises, Measurement of temperature-dependent thermal conductivity and viscosity of TiO₂-water nanofluids. *Experimental Thermal and Fluid Science*, 2009. 33(4): 706-714.
- Edel, Z. and A. Mukherjee, Experimental investigation of vapor bubble growth during flow boiling in a microchannel. *International Journal of Multiphase Flow*, 2011. 37(10): 1257-1265.
- Edel, Z. and A. Mukherjee, Experimental investigation of nanofluid flow boiling in a single microchannel. *Proceedings of the ASME International Summer Heat Transfer Conference*. July 8-12, 2012, Puerto Rico, USA.
- Edel, Z. and A. Mukherjee, Flow boiling dynamics of water and nanofluids in a single microchannel at different heat fluxes. *Proceedings of the ASME International Summer Heat Transfer Conference*. July 14-19, 2013, Minneapolis, MN, USA.
- Godson, L., et al., Enhancement of heat transfer using nanofluids – An overview. *Renewable and Sustainable Energy Reviews*, 2010. 14(2): 629-641.
- Henderson, K., et al., Flow-boiling heat transfer of R-134a based nanofluids in a horizontal tube. *International Journal of Heat and Mass Transfer*, 2010. 53(5-6): 944-951.

- Hetsroni, G., et al., Convective Boiling in Parallel Microchannels. *Microscale Thermophysical Engineering*, 2004. 8: 403-421.
- Hetsroni, G., et al., Two-phase flow patterns in parallel micro-channels. *International Journal of Multiphase Flow*, 2003. 29(3): 341-360.
- Ho, C. J., L. C. Wei, and Z. W. Li, An experimental investigation of forced convective cooling performance of a microchannel heat sink with Al₂O₃/water nanofluid. *Applied Thermal Engineering*, 2010. 30(2-3): 96-103.
- Huh, C., J. Kim, et al., Flow pattern transition instability during flow boiling in a single microchannel. *International Journal of Heat and Mass Transfer*, 2007. 50(5-6): 1049-1060.
- Huo, X., L. Chen, et al., Flow boiling and flow regimes in small diameter tubes. *Applied Thermal Engineering*, 2004. 24(8-9): 1225-1239.
- Jacobi, A. M. and J. R. Thome, Heat Transfer Model for Evaporation of Elongated Bubble Flows in Microchannels. *Journal of Heat Transfer*, 2002. 124(6): 1131-1136.
- Jung, J. Y., H. S. Oh, and H. Y. Kwak, Forced convective heat transfer of nanofluids in microchannels. *International Journal of Heat and Mass Transfer*, 2009. 52(1-2): 466-472.
- Kakac, S. and A. Pramuanjaroenkij, Review of convective heat transfer enhancement with nanofluids. *International Journal of Heat and Mass Transfer*, 2009. 52(13-14): 3187-3196.

- Kandlikar, S. G., Heat Transfer Mechanisms During Flow Boiling in Microchannels. *Journal of Heat Transfer*, 2004. 126(1): 8-16.
- Kandlikar, S. G., Nucleation characteristics and stability considerations during flow boiling in microchannels. *Experimental Thermal and Fluid Science*, 2006. 30(5): 441-447.
- Kandlikar, S. G., et al., Bubble nucleation and growth characteristics in subcooled flow boiling of water, in ASME Proceedings of the 32nd National Heat Transfer Conference. 1997. 11-18.
- Kandlikar, S. G., M. E. Steinke, et al., High-speed photographic observation of flow boiling of water in parallel mini-channels. 35th National Heat Transfer Conference (NHTC2001), 2001. Anaheim, CA, United States, American Society of Mechanical Engineers.
- Kandlikar, S. G., S. Garimella, et al., *Heat Transfer and Fluid Flow in Minichannels and Microchannels*. 2006, Kidlington, Oxford: ELSEVIER Ltd.
- Kim, H., H. S. Ahn, and M. H. Kim, On the Mechanism of Pool Boiling Critical Heat Flux Enhancement in Nanofluids. *Journal of Heat Transfer*, 2010. 132(6): 061501-11.
- Kim, H. D. and M. H. Kim, Effect of nanoparticle deposition on capillary wicking that influences the critical heat flux in nanofluids. *Applied Physics Letters*, 2007. 91(1): 014104-3.

- Kim, J., Y. T. Kang, and C. K. Choi, Analysis of convective instability and heat transfer characteristics of nanofluids. *Physics of Fluids*, 2004. 16(7): 2395-2401.
- Kim, S. J., et al., Alumina Nanoparticles Enhance the Flow Boiling Critical Heat Flux of Water at Low Pressure. *Journal of Heat Transfer*, 2008. 130(4): 044501-3.
- Kim, S. J., et al., Experimental Study of Flow Critical Heat Flux in Alumina-Water, Zinc-Oxide-Water, and Diamond-Water Nanofluids. *Journal of Heat Transfer*, 2009. 131(4): 043204-7.
- Kim, S. J., et al., Subcooled flow boiling heat transfer of dilute alumina, zinc oxide, and diamond nanofluids at atmospheric pressure. *Nuclear Engineering and Design*, 2010. 240(5): 1186-1194.
- Kim, S. J., et al., Surface wettability change during pool boiling of nanofluids and its effect on critical heat flux. *International Journal of Heat and Mass Transfer*, 2007. 50(19-20): 4105-4116.
- Kim, T. I., Y. H. Jeong, and S. H. Chang, An experimental study on CHF enhancement in flow boiling using Al₂O₃ nanofluid. *International Journal of Heat and Mass Transfer*, 2010. 53(5-6): 1015-1022.
- Kostarev, K., A. Viviani, and A. Zuev, Thermal and Concentrational Marangoni Convection at Liquid/Air Bubble Interface. *Journal of Applied Mechanics*, 2006. 73(1): 66-71.

- Krishnan, S., S. V. Garimella, et al., Towards a Thermal Moore's Law. IEEE Transactions on Advanced Packaging, 2007. 30(3): 462-474.
- Lee, H. J. and S. C. Yao, System Instability of Evaporative Microchannels, in ASME 2009 Heat Transfer Summer Conference. 2009, ASME: San Francisco, California.
- Lee, J. and I. Mudawar, Assessment of the effectiveness of nanofluids for single-phase and two-phase heat transfer in micro-channels. International Journal of Heat and Mass Transfer, 2007. 50(3-4): 452-463.
- Lee, M., L. S. L. Cheung, et al., Two-Phase Flow in Microchannel Heat Sink with Nearly Uniform Heat Flux Boundary Condition. Nano/Micro Engineered and Molecular Systems, 2006. NEMS '06. 1st IEEE International Conference on.
- Lee, P. C. and C. Pan, Boiling heat transfer and two-phase flow of water in a single shallow microchannel with a uniform or diverging cross section. Journal of Micromechanics and Microengineering, 2008. 18(2): 025005.
- Lee, P. C., F. G. Tseng, and C. Pan, Bubble dynamics in microchannels. Part I: single microchannel. International Journal of Heat and Mass Transfer, 2004. 47(25): 5575-5589.
- Li, H. Y., F. G. Tseng, and C. Pan, Bubble dynamics in microchannels. Part II: two parallel microchannels. International Journal of Heat and Mass Transfer, 2004. 47(25): 5591-5601.

- Li, J. and P. Cheng, Bubble cavitation in a microchannel. *International Journal of Heat and Mass Transfer*, 2004. 47(12-13): 2689-2698.
- Lu, C. T. and C. Pan, Stabilization of flow boiling in microchannel heat sinks with a diverging cross-section design. *Journal of Micromechanics and Microengineering*, 2008. 18(7): 075035.
- Meng, D. D. and C. J. Kim, An active micro-direct methanol fuel cell with self-circulation of fuel and built-in removal of CO₂ bubbles. *Journal of Power Sources*, 2009. 194(1): 445-450.
- Mukherjee, A., Contribution of thin-film evaporation during flow boiling inside microchannels. *International Journal of Thermal Sciences*, 2009. 48(11): 2025-2035.
- Mukherjee, A., Numerical Study of Conjugate Heat Transfer Due to Growth of a Vapor Bubble During Flow Boiling of Water in a Microchannel, in *ASME-JSME Thermal Engineering Summer Heat Transfer Conference*. 2007, ASME: Vancouver, British Columbia, Canada.
- Mukherjee, A., and Kandlikar, S. G., Numerical Simulation of growth of a vapor bubble during flow boiling of water in a microchannel. *Journal of Microfluidics and Nanofluidics*, 2005. 1(2): 137-145.
- Mukherjee, A. and S. G. Kandlikar, Numerical Study of an Evaporating Meniscus on a Moving Heated Surface. *Journal of Heat Transfer*, 2006. 128(12): 1285-1292.

- Mukherjee, A., and V. K. Dhir, Study of Lateral Merger of Vapor Bubbles During Nucleate Pool Boiling. *Journal of Heat Transfer*, 2004. 126(6): 1023-1039.
- Narayan, G. P., K. B. Anoop, and S. K. Das, Mechanism of enhancement/deterioration of boiling heat transfer using stable nanoparticle suspensions over vertical tubes. *Journal of Applied Physics*, 2007. 102(7): 074317-7.
- Peng, H., et al., Heat transfer characteristics of refrigerant-based nanofluid flow boiling inside a horizontal smooth tube. *International Journal of Refrigeration*, 2009. 32(6): 1259-1270.
- Peng, X. F., H. Y. Hu, and B. X. Wang, Boiling nucleation during liquid flow in microchannels. *International Journal of Heat and Mass Transfer*, 1998. 41(1): 101-106.
- Potash Jr, M. and P. C. Wayner Jr, Evaporation from a two-dimensional extended meniscus. *International Journal of Heat and Mass Transfer*, 1972. 15(10): 1851-1863.
- Qu, W. and I. Mudawar, Measurement and correlation of critical heat flux in two-phase micro-channel heat sinks. *International Journal of Heat and Mass Transfer*, 2004. 47(10-11): 2045-2059.
- Revellin, R., et al., Experimental investigation of velocity and length of elongated bubbles for flow of R-134a in a 0.5 mm microchannel. *Experimental Thermal and Fluid Science*, 2008. 32(3): 870-881.

- Squires, T. and S. Quake, Microfluidics: Fluid physics at the nanoliter scale. *Reviews of Modern Physics*, 2005. 77(3): 977.
- Steinke, M. E. and S. G. Kandlikar, Control and effect of dissolved air in water during flow boiling in microchannels. *International Journal of Heat and Mass Transfer*, 2004. 47(8-9): 1925-1935.
- Sujanani, M. and P. C. Wayner Jr, Transport processes and interfacial phenomena in an evaporating meniscus. *Chemical Engineering Communications*, 1992. 118:89-110.
- Thome, J. R. and A. Cioncolini, Recent Developments in Flow Boiling and Two-Phase Flow in Small Channels and Microchannels. *Heat Transfer Engineering*, 2010. 31(4): 225-256.
- Vafaei, S. and D. Wen, Effect of Gold Nanoparticles on the Dynamics of Gas Bubbles. *Langmuir*, 2010. 26(10): 6902-6907.
- Vafaei, S. and D. Wen, The effect of gold nanoparticles on the spreading of the triple line. *Microfluidics and Nanofluidics*, 2010. 8(6): 843-848.
- Vafaei, S., et al., The effect of nanoparticles on the liquid-gas surface tension of Bi₂Te₃ nanofluids. *Nanotechnology*, 2009. 20(18): 185702.
- Wang, G. and P. Cheng, An experimental study of flow boiling instability in a single microchannel. *International Communications in Heat and Mass Transfer*, 2008. 35(10): 1229-1234.

- Wang, G. and P. Cheng, Subcooled flow boiling and microbubble emission boiling phenomena in a partially heated microchannel. *International Journal of Heat and Mass Transfer*, 2009. 52(1-2): 79-91.
- Wang, G., P. Cheng, et al., Unstable and stable flow boiling in parallel microchannels and in a single microchannel. *International Journal of Heat and Mass Transfer*, 2007. 50(21-22): 4297-4310.
- Wang, X. Q. and A. S. Mujumdar, A review on nanofluids – Part I: Theoretical and numerical investigations. *Brazilian Journal of Chemical Engineering*, 2008. 25(4): 613-630.
- Wang, X. Q. and A. S. Mujumdar, A review on nanofluids – Part II: Experiments and applications. *Brazilian Journal of Chemical Engineering*, 2008. 25(4): 631-648.
- Wayner Jr, P. C., Y. K. Kao, and L. V. LaCroix, The interline heat-transfer coefficient of an evaporating wetting film. *International Journal of Heat and Mass Transfer*, 1976. 19(5): 487-492.
- Wen, D., On the role of structural disjoining pressure to boiling heat transfer of thermal nanofluids. *Journal of Nanoparticle Research*, 2008. 10(7): 1129-1140.
- Wen, D., et al., Review of nanofluids for heat transfer applications. *Particuology*, 2009. 7(2): 141-150.

- Wu, H.Y. and P. Cheng, Boiling instability in parallel silicon microchannels at different heat flux. *International Journal of Heat and Mass Transfer*, 2004. 47(17-18): 3631-3641.
- Wu, H. Y. and P. Cheng, Visualization and measurements of periodic boiling in silicon microchannels. *International Journal of Heat and Mass Transfer*, 2003. 46(14): 2603-2614.
- Wu, X., H. Wu, and P. Cheng, Pressure drop and heat transfer of Al₂O₃ – H₂O nanofluids through silicon microchannels. *Journal of Micromechanics and Microengineering*, 2009. 19(10): 105020.
- Xu, J., J. Zhou, et al., Static and dynamic flow instability of a parallel microchannel heat sink at high heat fluxes. *Energy Conversion and Management*, 2005. 46(2): 313-334.
- Xue, H. S., et al., Characteristic boiling curve of carbon nanotube nanofluid as determined by the transient calorimeter technique. *Applied Physics Letters*, 2007. 90(18): 184107-3.
- Yen, T. H., et al., Visualization of convective flow boiling heat transfer in single microchannels with different shaped cross-sections. *International Journal of Heat and Mass Transfer*, 2006. 49(21-22): 3884-3894.
- You, S. M., J. H. Kim, and K. H. Kim, Effect of nanoparticles on critical heat flux of water in pool boiling heat transfer. *Applied Physics Letters*, 2003. 83(16): 3374-3376.

- Zhang, L., E. N. Wang, et al., Phase change phenomena in silicon microchannels. International Journal of Heat and Mass Transfer, 2005. 48(8): 1572-1582.
- Zhang, T., et al., Ledinegg instability in microchannels. International Journal of Heat and Mass Transfer, 2009. 52(25-26): 5661-5674.
- Zhao, C. Y. and T. J. Lu, Analysis of microchannel heat sinks for electronics cooling. International Journal of Heat and Mass Transfer, 2002. 45(24): 4857-4869.